Available online at www.sciencedirect.com
SCIENCE DIRECT®
Ocean Modelling 12 (2006) 157–187
Ocean Modelling
www.elsevier.com/locate/ocemod

Evaluation and application of the ROMS 1-way embedding procedure to the central california upwelling system

Pierrick Penven [a,b,d,*], Laurent Debreu [a,c], Patrick Marchesiello [a,b,e], James C. McWilliams [a]

[a] *Institute of Geophysics and Planetary Physics, UCLA, 405 Hilgard Avenue, Los Angeles, CA 90095-1567, USA*
[b] *Institut de Recherche pour le Développement, 213 rue Lafayette, Paris, France*
[c] *Institut d'Informatique et Mathématiques Appliquées de Grenoble, Laboratoire de Modélisation et Calcul, BP 53, 38041 Grenoble Cedex 9, France*
[d] *Department of Oceanography, University of Cape Town, Rondebosch 7701, South Africa*
[e] *Unité Mixte de Recherche LEGOS, Centre IRD de Bretagne, BP 70, 29280 Plouzané, France*

Received 31 July 2003; received in revised form 18 May 2005; accepted 18 May 2005
Available online 28 June 2005

Abstract

What most clearly distinguishes near-shore and off-shore currents is their dominant spatial scale, O (1–30) km near-shore and O (30–1000) km off-shore. In practice, these phenomena are usually both measured and modeled with separate methods. In particular, it is infeasible for any regular computational grid to be large enough to simultaneously resolve well both types of currents. In order to obtain local solutions at high resolution while preserving the regional-scale circulation at an affordable computational cost, a 1-way grid embedding capability has been integrated into the Regional Oceanic Modeling System (ROMS). It takes advantage of the AGRIF (Adaptive Grid Refinement in Fortran) Fortran 90 package based on the use of pointers.

After a first evaluation in a baroclinic vortex test case, the embedding procedure has been applied to a domain that covers the central upwelling region off California, around Monterey Bay, embedded in a domain that spans the continental U.S. Pacific Coast. Long-term simulations (10 years) have been conducted to obtain mean-seasonal statistical equilibria. The final solution shows few discontinuities at the

* Corresponding author. Address: Department of Oceanography, University of Cape Town, Rondebosch 7701, South Africa. Tel.: +27 21 650 5315; fax: +27 21 650 3979.
E-mail address: pierrick.penven@ird.fr (P. Penven).

1463-5003/$ - see front matter
doi:10.1016/j.ocemod.2005.05.002

parent–child domain boundary and a valid representation of the local upwelling structure, at a CPU cost only slightly greater than for the inner region alone. The solution is assessed by comparison with solutions for the whole US Pacific Coast at both low and high resolutions and to solutions for only the inner region at high resolution with mean-seasonal boundary conditions.

Keywords: Ocean models; Boundary conditions; Embedding; Coastal upwelling; Mesoscale eddies; Eddy kinetic energy

Regional index terms: North America; West Coast; Central upwelling system; Monterey Bay

Geographic bounding coordinates: 35–41°N; 128–121°W

1. Introduction

Oceanic phenomena occur over a very large range of spatial scales. Processes includes turbulence at the scale of centimeters to meters, eddies and fronts at the scale of kilometers to hundreds of kilometers, and oceanic gyres and planetary waves at the scale of the oceanic basins. While micro-scale turbulence is usually parameterized by some closure scheme, strong interactions between mesoscale and large-scale processes require the resolution of disparate spatial scales. This is particularly true for coastal dynamics where near-shore currents develop on O(1–10) km due to boundary effects, while the dominant spatial scales offshore are O(30–1000) km.

To address the challenge of bridging the gap between near-shore and offshore dynamics, coastal modelers have developed unstructured-grid, finite-element models that allow non-uniform resolution (Lynch et al., 1996; Hervouet, 2000; Iskandarani et al., 2003) and, for finite-difference structured-grid models, stable open-boundary condition schemes (Marchesiello et al., 2001). The use of the finite-element models has largely been restricted to barotropic and tidal flows, estuaries, or short-term integrations, albeit with some exceptions (Lynch et al., 1996; Naimie, 1996; Hervouet, 2000; Hannah et al., 2001; Cushman-Roisin and Naimie, 2002; Iskandarani et al., 2003). While open-boundary conditions allow stable, multi-year simulations, the necessary large-scale boundary data, whether from measurements or a separate basin-scale model, is often either unavailable or of doubtful consistency with the local simulation. A way to circumvent this difficulty is to develop embedded- or nested-grid capabilities, where a hierarchy of embedded, structured-grid models are able to interact between each other.

For atmospheric models, embedding techniques have been employed successfully for many years (Kurihara et al., 1979). While 1-way embedding is the most common approach, 2-way, interactive grid coupling is used in many mesoscale meteorological models (Walko and Tremback, 2000; Stein et al., 2000; Dudhia and Bresch, 2002). (1-way coupling between the grid levels involves using information from coarser grids to influence the solution on finer grids, and 2-way coupling involves a back effect of fine-scale solutions on coarser ones.) With the adaptation of such mesoscale models to global applications, these embedding procedures are now available for global models (Dudhia and Bresch, 2002). In the context of non-hydrostatic mesoscale meteorology models, Clark and Hall (1991) proved that typical 2-way embedding (where coarse-grid values are interpolated to provide fine-grid boundary conditions and where the fine-grid solution is averaged on the coarse grid) is mathematically sound. More complex techniques can be

employed such as radiation of gravity waves at the fine grid boundaries, Newtonian relaxation for upscale exchange (Stein et al., 2000), or iterative pressure defect corrections (Clark and Hall, 1991).

For realistic regional oceanic models, the development of embedding procedures is still an important issue. Spall and Holland (1991) proposed a 2-level, 2-way embedding capability for the GFDL oceanic model. (N-level denotes the outer [parent] domain and $N-1$ levels of grid refinement on embedded subdomains [children].) They tested the procedure in idealized experiments on barotropic modons and baroclinic vortex with 3:1, 5:1, and even 7:1 grid-size ratios. By introducing topography and vertical refinement, Fox and Maskell (1995) improved the model and performed similar tests. They encountered noise generation when the fine and coarse topographies are not identical. For each of these cases, the embedding procedure did not respect integral mass, heat, or momentum conservation. A realistic, 2-way, embedded coastal simulation has been performed using the POM oceanic model (Oey and Chen, 1992) for the Norwegian Coastal Current. In this experiment, the embedded boundary condition are given by a "flow relaxation scheme" (Slørdal et al., 1994). No evaluation of the solution improvement by the embedding procedure was presented. The Kurihara et al. (1979) embedding method has been directly applied to a reduced-gravity, layered, oceanic model (Ginis et al., 1998), and this model has been applied to a large-scale simulation of the Tropical Pacific Ocean. To improve the continuity at the coarse/fine grid interface, Perkins et al. (1997) proposed to radiate the difference between the solutions. They also recommend enforcing mass conservation for long-term simulations. Their methods have been applied in short simulations (one week) for the Greenland–Iceland–Norwegian Sea and the Mediterranean Sea (Perkins and Smedstad, 1998). An offline, 1-way, embedding method (i.e., where boundary data for each model grid is stored at regular intervals longer than individual time steps) has been successfully employed using the POM oceanic model for the Kuroshio Current (Guo et al., 2003). In this solution, the higher resolution of a third embedded grid helped to produce a more plausible eastward veering and seasonal meridional migration of the current. Although this is not true embedding, the improvement of the solution at higher resolution in this case is encouraging. The theoretical framework developed by Heggelund and Berntsen (2002) for embedding techniques in simplified cases was used to show that, in the case of 2-way coupling, volume-conservation enforcement can create instabilities and that applying a Newtonian relaxation for the coarse-grid update by fine-grid values could stabilize the solution. Blayo and Debreu (1999) have designed and tested a method for adaptive mesh refinement (i.e., where embedded grid levels are generated depending on the evolution of the model solution). This technique showed good performances in idealized cases such as the barotropic modon and the double-gyre quasi-geostrophic circulation.

The present report focuses on the application of the AGRIF (Blayo and Debreu, 1999) embedding package to the ROMS model (Shchepetkin and McWilliams, 2005). For oceanic modeling, Sanderson (1998) demonstrated that, for a given accuracy, higher-order discretization is more efficient than low-order numerics with higher resolution. In ROMS, the higher-order numerical schemes, in addition to the conservative and constancy preserving baroclinic/barotropic mode coupling, result in a complex algorithmic structure (Shchepetkin and McWilliams, 2005). Herrnstein et al. (2005) presents an already complex 2-way embedding procedure for the case of a simple leapfrog time integration of the shallow-water equations. This is the reason why, in a first approach, we limit ourselves to the implementation and the evaluation of a 1-way embedding

procedure in ROMS. After a first evaluation in a baroclinic vortex test case, the procedure is tested in long-term, realistic simulations of the Central California upwelling regime. Its efficacy is evaluated by comparing different solutions with different grid resolutions and embedding procedures using statistical measures of this turbulent equilibrium regime.

2. Numerical method

2.1. ROMS

In this paper, the model employed is the Regional Oceanic Modeling System (ROMS). The reader is referred to Shchepetkin and McWilliams (2003) and to Shchepetkin and McWilliams (2005) for a more complete description.

ROMS solves the Primitive Equations in a rotating environment, based on the Boussinesq approximation and hydrostatic vertical momentum balance. ROMS is discretized in coastline- and terrain-following curvilinear coordinates. ROMS is a split-explicit, free-surface oceanic model, where short time steps are used to advance the surface elevation and barotropic momentum equations, with a much larger time step used for temperature, salinity, and baroclinic momentum. ROMS employs a special 2-way time-averaging procedure for the barotropic mode, which satisfies the 3D continuity equation. The baroclinic mode is discretized using a third-order accurate predictor (Leap-Frog) and corrector (Adams-Molton) time-stepping algorithm which allows a substantial increase in the permissible time-step size.

ROMS was originally designed to be optimized on shared-memory parallel computer architectures. Parallelization is done by two-dimensional subdomain partitioning. Multiple subdomains can be assigned to each processor to optimize the use of processor cache memory. This allows super-linear scaling with performance growth even faster than the number of CPUs. ROMS has been also ported successfully to distributed-memory platforms.

In combination with an accurate time-stepping, the third-order, upstream-biased advection scheme implemented in ROMS allows the generation of steep gradients, enhancing the effective resolution of the solution for a given grid size (Shchepetkin and McWilliams, 1998). The explicit lateral viscosity is null everywhere in the model domain except in sponge layers near the open boundaries where it increases smoothly close to the lateral open boundaries. A non-local, K-Profile Parameterization (KPP) boundary-layer scheme (Large et al., 1994) parameterizes the subgrid-scale vertical mixing processes.

2.2. 1-Way embedding procedure

2.2.1. AGRIF

The method chosen for embedded gridding takes advantage of the AGRIF (Adaptive Grid Refinement in Fortran) package (Debreu and Blayo, 2003; Debreu and Vouland, 2003). AGRIF is a Fortran 90 package for the inclusion of adaptive mesh refinement (AMR) features within a finite-difference numerical model. The package is based on the use of pointers which minimizes the changes in the original numerical model. Regardless of the possibility of adaptive refinement (i.e the automatic generation and evolution of high-resolution subdomains in response to dynamical

criteria), one of the major advantages of AGRIF in static-grid embedding is the ability to manage an arbitrary number of fixed grids and an arbitrary number of embedding levels.

The pointers were originally implemented in C language, and they have recently been added in Fortran 90. A pointer variable is able to address different locations in the memory during the computation. This is what is done in our embedding procedure, when skipping from the computation on one grid to the computation on another grid. In AGRIF, a unique set of pointers will address successively the memory locations corresponding to the variables of the different grids.

The embedding procedure has been implemented so as to preserve the efficiency of ROMS on parallel super-computers.

2.2.2. Time stepping

A recursive integration procedure manages the time evolution for the child grids during the time step of the parent grids. ROMS resolves explicitly the external mode. To preserve the CFL criterion for a typical coefficient of refinement r_{coef} (say, a factor of 3 for a 5 km resolution grid embedded in a 15 km grid), for each parent time step the child must be advanced using a time step divided by the coefficient of refinement as many time as necessary to reach the time of the parent. For simple 2-level embedding, the procedure is as follows:

(1) Advance the parent grid by one parent time step.
(2) Interpolate the relevant parent variables in space and time to get the boundary conditions for the child grid.
(3) Advance the child grid by as many child time steps as necessary to reach the new parent model time.

The recursive approach allows the specification of any number of embedding level. The both conservative and constancy-preserving ROMS time step (Shchepetkin and McWilliams, 2005) significantly complicates the embedding procedure. The following summarizes the procedure that was developed by Shchepetkin and McWilliams (2005) to perform a model step from the baroclinic time index n to time index $n+1$:

(1) A predictor scheme (Shchepetkin and McWilliams, 2005, LF-AM3) advances the baroclinic equations to $n+\frac{1}{2}$. The right-hand side terms are computed for $n+\frac{1}{2}$ and converted into baroclinic-to-barotropic forcing terms.
(2) The barotropic variables are advanced by several significantly shorter "fast" time steps to almost $n+\frac{3}{2}$. Using a specific filtering procedure, the "slow-time quantities" for the vertically integrated current vectors ($\mathbf{U}$) are obtained for $n+\frac{1}{2}: \langle\langle \overline{\mathbf{U}} \rangle\rangle_{n+\frac{1}{2}}$, and for $n+1: \langle \overline{\mathbf{U}} \rangle_{n+1}$ (Shchepetkin and McWilliams, 2005).
(3) These values are then employed to advance the baroclinic equations from n to $n+1$ (corrector step).

To obtain a temporal refinement in the context of time splitting, we have chosen to locate the parent–child coupling at the baroclinic level. The baroclinic prognostic variables (i.e the 2 horizontal momentum components, temperature and salinity) are bilinearly interpolated along each sigma level and linearly interpolated in time for each time step of the child model, for both

$n^{\text{child}} + \frac{1}{2}$ and $n^{\text{child}} + 1$. This implies that the parent and child sigma levels (i.e. the bottom topographies) must correspond in the vicinity of the parent–child boundary. In the presence of land masking, the nearest non-masked values are used in the interpolation procedure. For the baroclinic variables, we used a Dirichlet (clamped) condition for the child boundary conditions.

2.2.3. Barotropic mode

For the barotropic mode, two methods were retained for the child boundary conditions:

(1) *Storage*: we store in specific arrays the components of the parent barotropic transport at the parent–child boundary for each parent barotropic time step.
(2) *Time average*: since $\langle\langle\overline{\mathbf{U}}\rangle\rangle_{n+\frac{1}{2}}$ and $\langle\overline{\mathbf{U}}\rangle_{n+1}$ are the barotropic vectors involved in the coupling with the baroclinic mode, we base the parent–child exchange on these elements.

The first method (storage) has the advantage to be the most accurate for the propagation of external gravity waves. This might be of importance in the case of tidal studies, when using a large baroclinic time step. The inconvenient is that the storage in extra arrays might affect model performances on specific parallel platforms. Because it needs to explicitly store the boundary child values throughout the parent time-step, this method allows solely the definition of one child grid per parent grid. Nevertheless, it is still possible to define multiple levels of embedding.

In the second method (time average) we compute the barotropic fluxes ($\mathbf{U}^{\text{child}}$) at the child boundary from the slow time parent barotropic transports: $\langle\overline{\mathbf{U}}\rangle_n^{\text{parent}}$, $\langle\langle\overline{\mathbf{U}}\rangle\rangle_{n+\frac{1}{2}}^{\text{parent}}$ and $\langle\overline{\mathbf{U}}\rangle_{n+1}^{\text{parent}}$. To conserve mass throughout the length of the parent time step in the context of the ROMS time-stepping algorithm, $\mathbf{U}^{\text{child}}$ should be defined as

$$\begin{aligned}
&\mathbf{U}^{\text{child}} = \langle\overline{\mathbf{U}}\rangle_n^{\text{parent}}, \quad \text{for } t = t_n^{\text{parent}},\\
&\mathbf{U}^{\text{child}} = \langle\overline{\mathbf{U}}\rangle_{n+1}^{\text{parent}}, \quad \text{for } t = t_{n+1}^{\text{parent}},\\
&\frac{1}{t_{n+1}^{\text{parent}} - t_n^{\text{parent}}} \int_{t_n^{\text{parent}}}^{t_{n+1}^{\text{parent}}} \mathbf{U}^{\text{child}}\,\mathrm{d}t = \langle\langle\overline{\mathbf{U}}\rangle\rangle_{n+\frac{1}{2}}^{\text{parent}},
\end{aligned} \tag{1}$$

where t is the model time, t_n^{parent} is the time at the start of the parent baroclinic time step, and t_{n+1}^{parent} is the time at the end of the parent baroclinic time step. These conditions can be satisfied using a second-order polynomial. Using $t' = \frac{t - t_n^{\text{parent}}}{t_{n+1}^{\text{parent}} - t_n^{\text{parent}}}$, we obtain

$$\begin{aligned}
\mathbf{U}^{\text{child}} = {} & 3(\langle\overline{\mathbf{U}}\rangle_n^{\text{parent}} - 2\langle\langle\overline{\mathbf{U}}\rangle\rangle_{n+\frac{1}{2}}^{\text{parent}} + \langle\overline{\mathbf{U}}\rangle_{n+1}^{\text{parent}})t'^2 + 2(-2\langle\overline{\mathbf{U}}\rangle_n^{\text{parent}} + 3\langle\langle\overline{\mathbf{U}}\rangle\rangle_{n+\frac{1}{2}}^{\text{parent}}\\
& - \langle\overline{\mathbf{U}}\rangle_{n+1}^{\text{parent}})t' + \langle\overline{\mathbf{U}}\rangle_n^{\text{parent}}.
\end{aligned} \tag{2}$$

As a first approximation, $\mathbf{U}^{\text{child}}$ is temporally averaged over each child baroclinic time step (n'). The term used to force the child boundary is thus kept constant throughout the duration of a child baroclinic time step,

$$\overline{\mathbf{U}}_{n'}^{\text{child}} = \frac{\int_{t_{n'}^{\text{child}}}^{t_{n'+1}^{\text{child}}} \mathbf{U}^{\text{child}}\,\mathrm{d}t}{t_{n'+1}^{\text{child}} - t_{n'}^{\text{child}}}, \tag{3}$$

where $t^{\text{child}}_{n'}$ is the time at the start of the baroclinic child step, and $t^{\text{child}}_{n'+1}$ is the time at the end of the baroclinic child step. For any time-filtering procedure used in ROMS, this ensures

$$\frac{1}{r_{\text{coef}}}\sum_{n'=1}^{r_{\text{coef}}}\langle\langle\overline{\mathbf{U}}\rangle\rangle^{\text{child}}_{n'+\frac{1}{2}} = \langle\langle\overline{\mathbf{U}}\rangle\rangle^{\text{parent}}_{n+\frac{1}{2}}, \tag{4}$$

where r_{coef} is the refinement coefficient. In ROMS, $\langle\langle\overline{\mathbf{U}}\rangle\rangle^{\text{parent}}_{n+\frac{1}{2}}$ is responsible for the change in sea level between the two consecutive slow-time steps (Shchepetkin and McWilliams, 2005), the total sea level variation after one parent baroclinic time step ($\Delta\eta^{\text{parent}}$) is then consistent between the parent and the child grid,

$$\Delta\eta^{\text{parent}} = -\Delta t\nabla.\langle\langle\overline{\mathbf{U}}\rangle\rangle^{\text{parent}}_{n+\frac{1}{2}} = -\frac{\Delta t}{r_{\text{coef}}}\sum_{n'=1}^{r_{\text{coef}}}\nabla.\langle\langle\overline{\mathbf{U}}\rangle\rangle^{\text{child}}_{n'+\frac{1}{2}}, \tag{5}$$

where Δt is length of the parent baroclinic time step.

For both methods, horizontal bilinear interpolation of fluxes does not guaranty volume conservation at the parent–child boundary. An enforcement of volume conservation is applied locally to the transport across the boundaries ($U_\perp$) for each parent grid element (Γ) along the parent–child boundary,

$$U^{\text{child}}_{\perp\text{new}} = U^{\text{child}}_{\perp\text{fine}} + \int_\Gamma U^{\text{child}}_{\perp\text{coarse}}\,\mathrm{d}l - \int_\Gamma U^{\text{child}}_{\perp\text{fine}}\,\mathrm{d}l, \tag{6}$$

where $U^{\text{child}}_{\perp\text{new}}$ is the corrected cross-boundary transport, $U^{\text{child}}_{\perp\text{fine}}$ is the cross-boundary transport after the spatial interpolation and $U^{\text{child}}_{\perp\text{coarse}}$ is the cross-boundary transport before the spatial interpolation.

To apply the interpolated barotropic transport at the child boundaries, after testing several different techniques, we selected the Flather radiation condition (Flather, 1976) as an alternative to the Dirichlet boundary conditions. This condition is obtained by combining the Sommerfeld equation (using surface gravity wave speed) for the flow across the boundary with an approximation of the continuity equation,

$$\bar{u}_\perp = \frac{U^{\text{child}}_{\perp\text{new}}}{H} \pm \sqrt{\frac{g}{H}}(\eta_{\text{child}} - \eta_{\text{parent}}), \tag{7}$$

where $\bar{u}_\perp$ is the boundary value for the cross-shore barotropic current, H is the local depth, g is gravity acceleration and η is the free surface elevation. The sign ($\pm$) depends on the position of the boundary: negative for a western or southern boundary, positive for an eastern or northern boundary. This method can be described as the prescription of the incoming characteristic for the shallow-water equations (Blayo and Debreu, 2005). This ensures a near conservation of mass and energy through the open boundary (Blayo and Debreu, 2005). In addition, the radiation conditions designed by Marchesiello et al. (2001) are applied on the alongshore barotropic velocities and the sea-surface elevation.

2.2.4. Topography

A notorious problem for terrain-following atmospheric and oceanic models is the so-called sigma-coordinate pressure-gradient error (Haney, 1991). While progress has been recently made

to ameliorate this problem (Shchepetkin and McWilliams, 2003), in realistic simulations the bottom topography still needs to be sufficiently smooth to prevent spurious circulations. Smoothing is more important at low resolution. This might introduce differences between the topographies used by the parent and child. To prevent discontinuities at the interfaces between the different grid levels, the child's topography is smoothly connected to the parent's topography using the relation,

$$h^{\text{child}} = \alpha h^{\text{parent}} + (1-\alpha)h^{\text{fine}}, \tag{8}$$

where h^{child} is the bottom topography of the child grid, h^{parent} is the bottom topography of the parent grid, h^{fine} is a high-resolution bathymetry, and α is a parameter going in a few grid steps from zero to one when approaching the lateral boundaries of the child grid.

The child topography is kept concomitant with the parent topography for the 2 first parent grid points close to the parent–child boundary. In this band, a special treatment is also applied to enforce the child grid to have the same vertical section and the same volume as each corresponding parent grid cell. In association with volume conservation, this insures tracer conservation.

2.3. Baroclinic vortex test case

The ROMS embedding procedure is first evaluated in an idealized case study. Because the aim is to address the dynamics of the California Current System, known to host a collection of eddies generated through barotropic and baroclinic instability processes (Marchesiello et al., 2003), the baroclinic vortex described by Spall and Holland (1991) (hereafter SH91) is a suitable test case for our embedding procedure. The embedded solutions are evaluated against a single-grid, high-resolution model calculation.

2.3.1. Initial condition and model configuration

As described by SH91, the vortex is initialized by a Gaussian surface pressure distribution $P(z=0)$ with a maximum surface geostrophic velocity ($u_{\max}$) of 1 m s^{-1} and a horizontal e-folding scale (λ) of 60 km. The surface dynamic pressure takes the form,

$$P(z=0) = P_0 \mathrm{e}^{-\frac{x^2+y^2}{2\lambda^2}}, \tag{9}$$

where P_0 is defined by the maximum geostrophic velocities,

$$P_0 = \rho_0 f_0 u_{\max} \lambda \sqrt{e}. \tag{10}$$

As a difference with SH91, instead of doing somehow a two-layer model, we took advantage of the vertical discretization of ROMS. We designed a baroclinic vortex in the presence of a continuous background stratification, with no motion below a specific level: $z=-H_1$. Hence, the dynamic pressure can be written as

$$P = F(z)\mathrm{e}^{-\frac{x^2+y^2}{2\lambda^2}}, \tag{11}$$

where $F(z)$ is a function such as

$$\begin{aligned} F(0) &= P_0, \\ F(-H_1) &= 0. \end{aligned} \tag{12}$$

In addition, to ensure no motion below $z = -H_1$, the density should be horizontally uniform for $z \leqslant -H_1$. The density anomaly, associated to the dynamic pressure by the hydrostatic balance, should then vanish for $z = -H_1$. This adds the additional constraint for F,

$$\frac{\partial F(-H_1)}{\partial z} = 0. \tag{13}$$

A simple solution for (11)–(13) is

$$P = P_0 \frac{H_1 - 1 + z + \mathrm{e}^{-(z+H_1)}}{H_1 - 1 + \mathrm{e}^{-H_1}} \mathrm{e}^{-\frac{x^2+y^2}{2\lambda^2}}. \tag{14}$$

A background linear stratification is added to the density anomaly. Hence, the total density takes the form of

$$\begin{aligned} \rho &= \rho_0 - \frac{\rho_0 N^2}{g} z - \frac{P_0}{g} \frac{1 - \mathrm{e}^{-(z+H_1)}}{H_1 - 1 + \mathrm{e}^{-H_1}} \mathrm{e}^{-\frac{x^2+y^2}{2\lambda^2}}, \quad \text{for } z > -H_1, \\ \rho &= \rho_0 - \frac{\rho_0 N^2}{g} z, \quad \text{for } z \leqslant -H_1, \end{aligned} \tag{15}$$

where N is the Brünt–Vaissala frequency and g is the gravity acceleration. The density is related to the temperature (T) by a linear relation,

$$\rho = 1030 - 0.28T. \tag{16}$$

The sea-surface elevation (ς) is derived from $P(z = 0)$,

$$\varsigma \simeq \frac{P_0 \mathrm{e}^{-\frac{x^2+y^2}{2\lambda^2}}}{\rho(z=0)g}. \tag{17}$$

The initial horizontal velocities are in geostrophic equilibrium with the pressure field. With this initialization, using a sufficient vertical resolution, we expect to prevent the generation of the spurious fast barotropic modes which perturbed SH91's solutions.

For most of the model parameters, we kept the values used by SH91. The grids are square, on a flat bottom ($H_0 = 5000$ m), using the β-plane approximation centered around 38.5° N. The parent grid domain is 1800 km × 1800 km, while the child grid domain is approximately 580 km × 580 km. Different from SH91, we used 10 evenly spaced vertical levels, no horizontal viscosity (unless specified in specific sponge areas), no vertical viscosity, and no bottom friction. The level of nomotion is $H_1 = 2500$ m. The Brünt–Vaissala frequency is fixed at $N = 0.003\ \mathrm{s}^{-1}$ to obtain a "realistic" vertical temperature profile. The model parameters are summarized on Table 1. The names V1, V3.x, V5 and V7 represent respectively embedded simulations using grid ratios of 1:1, 3:1, 5:1 and 7:1. Table 1 lists which method is used for the barotropic mode: "storage" or "time average" (see Section 2.2.3), and also if the Flather radiation condition is applied for the barotropic boundary conditions. If a sponge is defined (experiences V3.4, V3.5 and V3.6), the horizontal Laplacian mixing coefficient smoothly increases from 0 to $v_{\max}$ in the first 10 grid points close to each boundary.

Table 1
Parent and child model parameters for the baroclinic vortex experiments

Run	$L \times M$ (parent)	δ_x [km] (parent)	dt [s] (parent)	$L \times M$ (child)	Fast mode	Radiation	Sponge (v_{max}) [m^2 s^{-1}]
V1	180×180	10	960	58×58	Time average	None	0
V3.1	60×60	30	2880	58×58	Time average	None	0
V5	36×36	50	4800	56×56	Time average	None	0
V7	25×25	70	6720	50×50	Time average	None	0
V3.2	60×60	30	2880	58×58	Storage	None	0
V3.3	60×60	30	2880	58×58	Storage	Flather	0
V3.4	60×60	30	2880	58×58	Storage	Flather	200
V3.5	60×60	30	2880	58×58	Storage	Flather	400
V3.6	60×60	30	2880	58×58	Storage	Flather	800

For all experiments the child horizontal resolution is 10 km and the child time step is 960 s.

2.3.2. Model solutions

As shown by SH91, the evolution of the vortex in the reference solution (V1) is portrayed for the whole domain for the sea-surface elevation and for the sea-surface temperature (Fig. 1). As expected, the eddy is propagating steadily to the southwest. In this simulation, the eddy seems

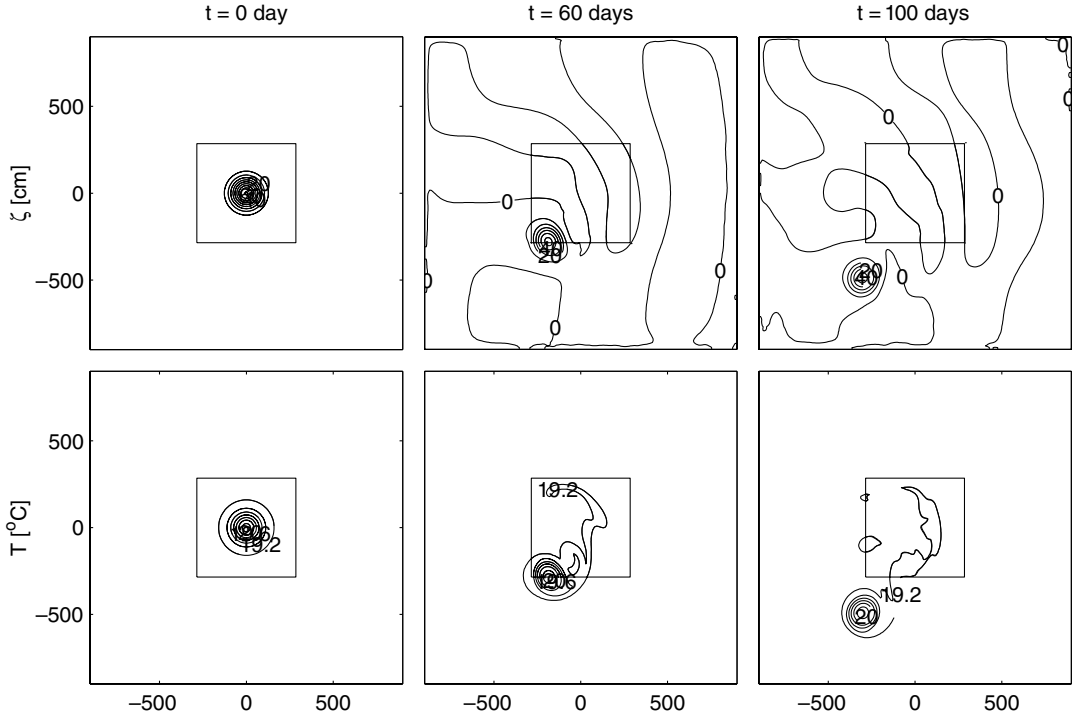

Fig. 1. Reference solution (V1) for the baroclinic vortex for days 0, 60 and 100. Top: sea surface elevation [cm], the contour interval is 10 cm. Bottom: sea surface temperature [°C], the contour interval is 0.2 °C. The box represents the embedded domain, in this case using the same resolution as the parent grid (10 km).

to move slightly more rapidly than in SH91's reference solution. The free surface elevation (which can be seen as an approximation of the streamfunction for the surface flow) accounts for the fast modes. Because of the adjusted initialization, different from the streamfunction shown by SH91, both sea-surface temperature and sea surface height retain the eddy signature as it moves across the model domain.

The sea-surface temperature, the surface elevation and their differences to the reference solution are presented for the child grid of experiment V3.5 (Fig. 2). At day 30, the eddy starts to interact with the lateral boundary. Until this time, for both sea-surface temperature and sea-surface elevation, the differences between V3.5 and the reference remain almost unnoticeable. At day 60, the eddy overlaps the child boundary. At this time, the difference between V3.5 and the reference reaches a maximum. The eddy in the V3.5 parent solution is slower than in the reference solution, takes an elliptic shape and fades away rapidly. In the case of 1-way nesting, the use of specific radiations schemes with sponges layers might reduce the generation of parent–child inconsistencies at the child boundaries, but this won't prevent the introduction of biases induced by weaknesses of the parent solution. Therefore the differences between the fine grid solution and the

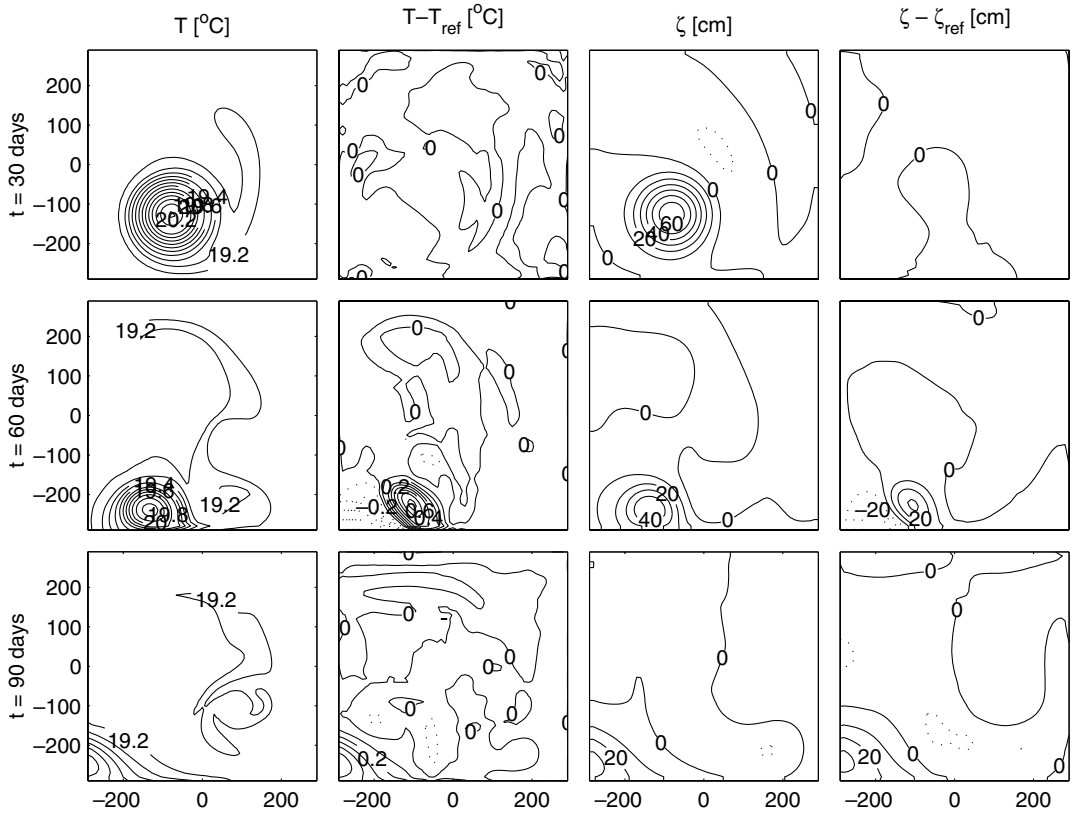

Fig. 2. Embedded solution (V3.5, sea surface temperature [°C] and sea surface elevation [cm]), and its differences with the reference solution (V1) in the child grid region for days 30, 60 and 90. The contour interval for temperature is 0.1 °C. The contour interval for the surface elevation is 10 cm.

reference become relatively important at day 60. In comparison to the reference, the eddy is delayed and distorted. This behavior is noticeable for both temperature and sea-surface elevation. Note that while in SH91's experiments the streamfunction departs from the reference solution throughout the whole child domain, in our model, the errors in sea-surface elevation are mostly confined to where the eddy interacts with the boundary. In the reference solution, at day 90 the eddy has totally vanished from the child domain (Fig. 1), whereas in V3.5 there is still a signature that slowly disappears in the southwest corner of the child grid (Fig. 2).

The differences between the reference and the child-grid solutions are summarized as RMS errors on Fig. 3. As in SH91 the errors have been normalized by the RMS of the initial perturbation fields. Errors for V1 are small for both sea-surface temperature and sea-surface elevation (Fig. 3). In agreement with what was explained in the previous paragraph, the error for sea-surface temperature in V3.1 (Fig. 3a) increases with the eddy approaching the boundary, to reach a maximum of 60% at day 60. The error diminishes as the eddy moves away from the child grid. It is below 25% at day 100. SH91's solution presents the same pattern although the maximum error for temperature attains only 18% for V3. Nevertheless, after 100 days, the difference between their level of error (~14%) and our level (~25%) has noticeably decreased. For the case of sea-surface elevation (Fig. 3b), before day 60, the error follows the same pattern as for the temperature. After day 60, it reaches a plateau of about 50%. Because the solution is not polluted by reflecting barotropic waves, there is a net improvement in comparison to the transport streamfunction shown by SH91. V5 and V7 present together almost the same pattern (Fig. 3). In the case of 1-way nesting, the eddy in the parent grids for V5 and V7 disappears rapidly. Hence the boundary conditions for the child grid in V5 and V7 after 60 days are almost equivalent to the application of a constant background field.

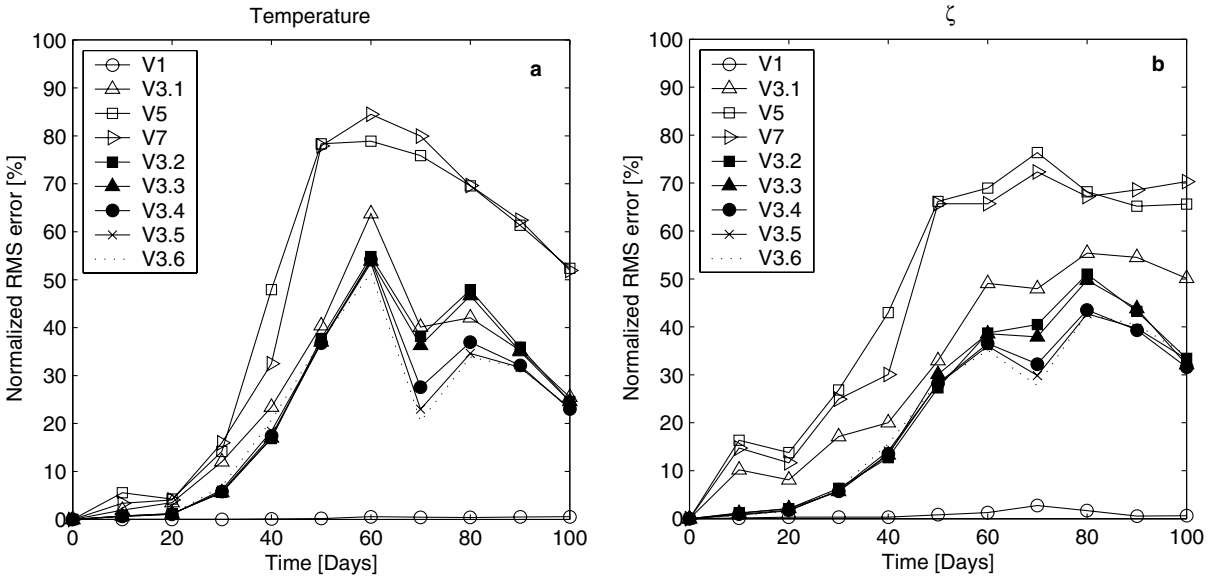

Fig. 3. Normalized RMS difference (%) between the different embedded solutions and the reference solution in the child grid region: (a) sea surface temperature; (b) sea surface elevation.

In comparison to V3.1, the "storage" method for the barotropic variables (V3.2) improves the solution, as well as the addition of a Flather radiation condition (V3.3) and lateral sponge layers (V3.4, V3.5 and V3.6). Three different values of v_{max} are tested: 200 $m^2 s^{-1}$ (V3.4), 400 $m^2 s^{-1}$ (V3.5) and 800 $m^2 s^{-1}$ (V3.6). V3.5 results in slightly less error than V3.4 (Fig. 3), due to a smoother solution close to the boundaries. Increasing the value of the sponge (V3.6) did not significantly improve the boundaries' behavior. In V3.6, the sponges start to affect the inner solution. This is noticeable as a slight error increase around day 40 on Fig. 3. In experiments V3.4, V3.5 and V3.6, the remaining errors are for the greater part unrelated to numerical noise generated at the boundary, but they are rather caused by eddy distortions induced by weaknesses in the parent solution.

In the case of 1-way embedding, from all the methodologies that we have tested, V3.5 ("storage" method + Flather radiation condition + sponge with $v_{max} = 400\ m^2 s^{-1}$) appears to be the most efficient. The "storage" method reduces the parent–child inconsistencies for the barotropic mode, the Flather radiation condition helps the evacuation of the fast moving waves, and the sponges layers prevent the generation of discontinuities close to the boundaries. For V3.5, the maximum level of errors reduces to 53% for the temperature and to 43% for the sea-surface elevation. These levels can be compared to the maximum errors of 18% for the temperature and 72% for the streamfunction obtained in the case of 2-way embedding by SH91 for V3.

The embedding method used in V3.5 are employed for the following realistic experiments. The "baroclinic vortex test bed" should also be useful for the future evaluation of new developments.

3. The 15 + 5 central upwelling model

The AGRIF embedding procedure has been already tested in process studies (Blayo and Debreu, 1999) and in basin-scale simulations (Debreu, 2000). The aim of this paper is to assess the ability of the embedding procedure in ROMS to improve the resolution of coastal solutions, especially for the dynamics of upwelling systems. In this framework, the embedding has been applied to the central upwelling of California, in a region including Monterey Bay, one of the most studied areas of the Pacific Coast of the United States. The central upwelling of the Pacific Coast occurs in a region extending from Point Conception in the South to Cape Mendocino in the North. Winds in this area are often favorable to upwelling all year long. Associated with the upwelling are an equatorward surface current (the California Current) and a poleward undercurrent. The California Current interacts with coastline protrusions such as Cape Mendocino, Point Arena, or Point Reyes to generate local maxima for eddy energy in Northern California. Another important topographic feature of the region is the Monterey Bay Canyon.

3.1. Configuration

To test the capabilities of the embedding procedure, the child model (i.e., the high-resolution embedded grid) is chosen as a portion of the high-resolution (5 km) model (referred to hereafter as USWC) of the West Coast of the United States, analyzed in Marchesiello et al. (2003). The configuration includes only one embedded grid with finer resolution (i.e., 2-level embedding). The parent model is fully congruent with the USWC domain. It has a resolution 3 times coarser

than the child (i.e., 15 km). Using a coefficient of refinement of 3, the child grid has a resolution of 5 km, identical to the USWC configuration.

The parent model has 84×169 grid points in the horizontal and 20 vertical levels. The time step is approximately 45 min. Three open boundaries connect the model domain to open-ocean data. An oblique radiation condition is applied on outgoing signals, but if the information propagation direction is inward, the model solution is nudged toward monthly mean climatological data (Levitus and Boyer, 1994; Levitus et al., 1994). While the explicit lateral viscosity is zero inside the model domain, it increases following a cosine curve within the 150 km close to an open boundary and attains a maximum value of 300 $m^2 s^{-1}$. This prevents the generation of solution discontinuities in the vicinity of the open boundaries. A global volume-conservation constraint is applied on the lateral barotropic fluxes around the parent domain periphery (Marchesiello et al., 2001).

Embedded within the parent grid, the child model has a domain of 1000 km alongshore times approximately 500 km cross-shore. It goes from Point Conception in the south to Cape Mendocino in the north (Fig. 4). It has 94×190 grid points in the horizontal and, as the parent, 20 vertical levels. The time step is approximately 15 min. The parent grid provides the lateral boundary conditions for the child at each baroclinic time step. Only the 1-way embedding capability is tested in this paper, so the parent model is not affected by the presence of the child grid. In a band of 50 km close to the lateral grid boundary, the horizontal viscosity increases from 0 to maximum value of 50 $m^2 s^{-1}$ to ensure a smooth transition between the different grid levels.

Parent and child models are both forced at the surface with the same monthly mean climatology from COADS data set (Da Silva et al., 1994), both are started from rest using the same initial

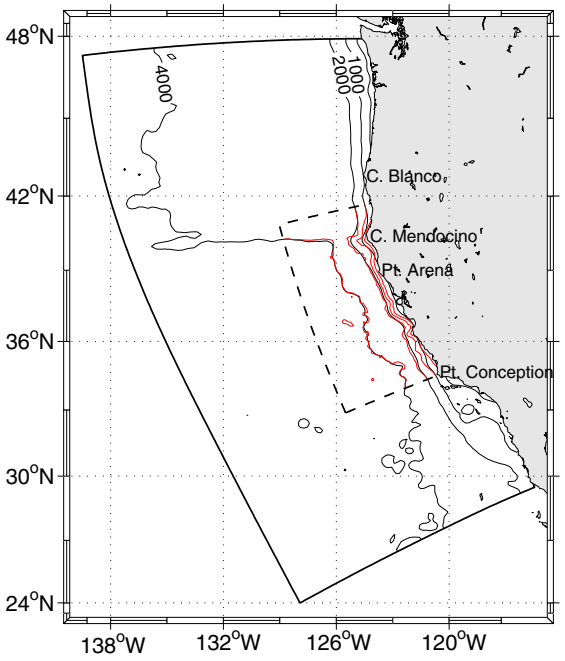

Fig. 4. The $15 + 5$ central upwelling model bottom topographies. The black contours represent the parent model topography. The red contours represent the child topography.

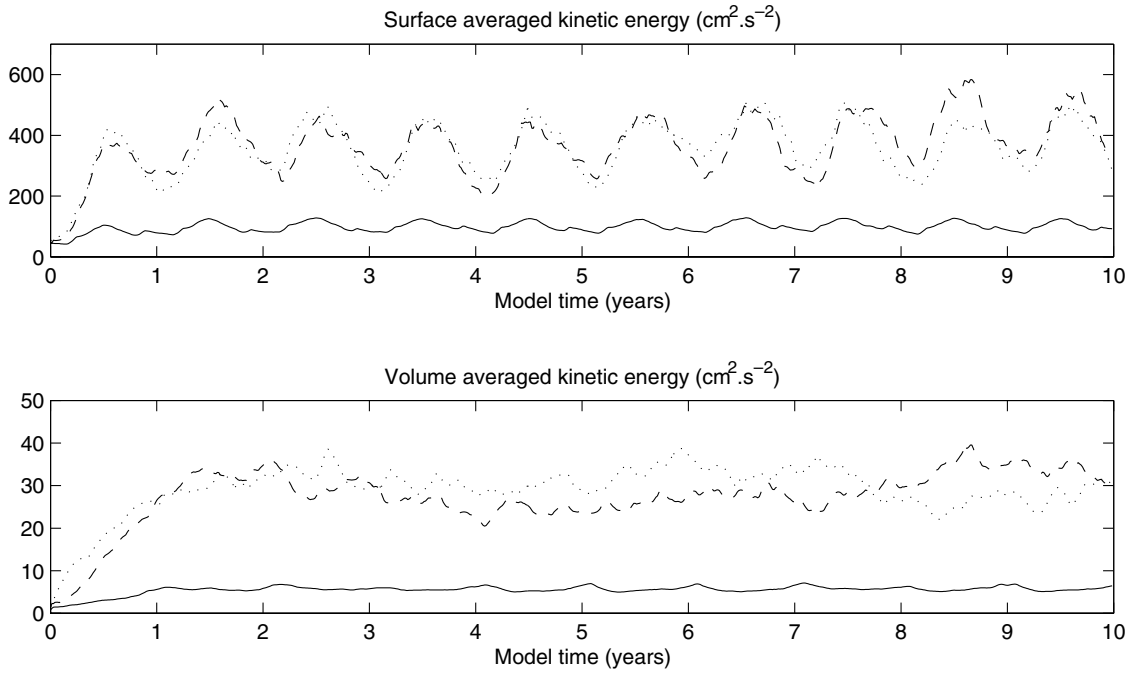

Fig. 5. Top: time evolution of the surface-averaged kinetic energy ($cm^2\ s^{-2}$). Bottom: time evolution of the volume-averaged kinetic energy ($cm^2\ s^{-2}$). The continuous line represents a subdomain of the parent model that covers the child grid; the dotted line represents the child model using the Flather boundary condition; and the dashed line represents the child model using clamped boundary conditions.

condition in temperature (Levitus and Boyer, 1994) and salinity (Levitus et al., 1994). For the bottom topography, although both parent and child grids are based on the same dataset (Smith and Sandwell, 1997), the different degree of smoothing required induces significant differences between the 2 grids in their representation of the shelf and the slope (Fig. 4).

As for the USWC model, a 10-year simulation is made to reach a nearly repeating annual cycle. Fig. 5 depicts the time variations of surface-averaged (Fig. 5-top) and volume-averaged (Fig. 5-bottom) kinetic energy. For each grid level, after a spin-up of approximately 2 years, the solution attains a statistical equilibrium. A strong seasonal cycle is present at the surface. The model solutions are analyzed from year 3 to year 10. The level of kinetic energy in the child model is more than three times higher than the level in the parent model due to more vigorous mesoscale flows.

3.2. Parent–child boundary behavior

The behavior of the embedding procedure is illustrated on Fig. 6. This image represents the sea-surface temperature (here the temperature of the first grid level) (Fig. 6a), the surface vorticity (Fig. 6b), the temperature at 100 m (Fig. 6c) and the vorticity at 100 m (Fig. 6d). Fig. 6a depicts a typical summer situation with a strong upwelling front from which a sequence of filaments detaches and extends 10–100s km offshore. While steeper sea-surface temperature gradients are apparent within the child domain, few discontinuities appears at its lateral boundaries. In the case

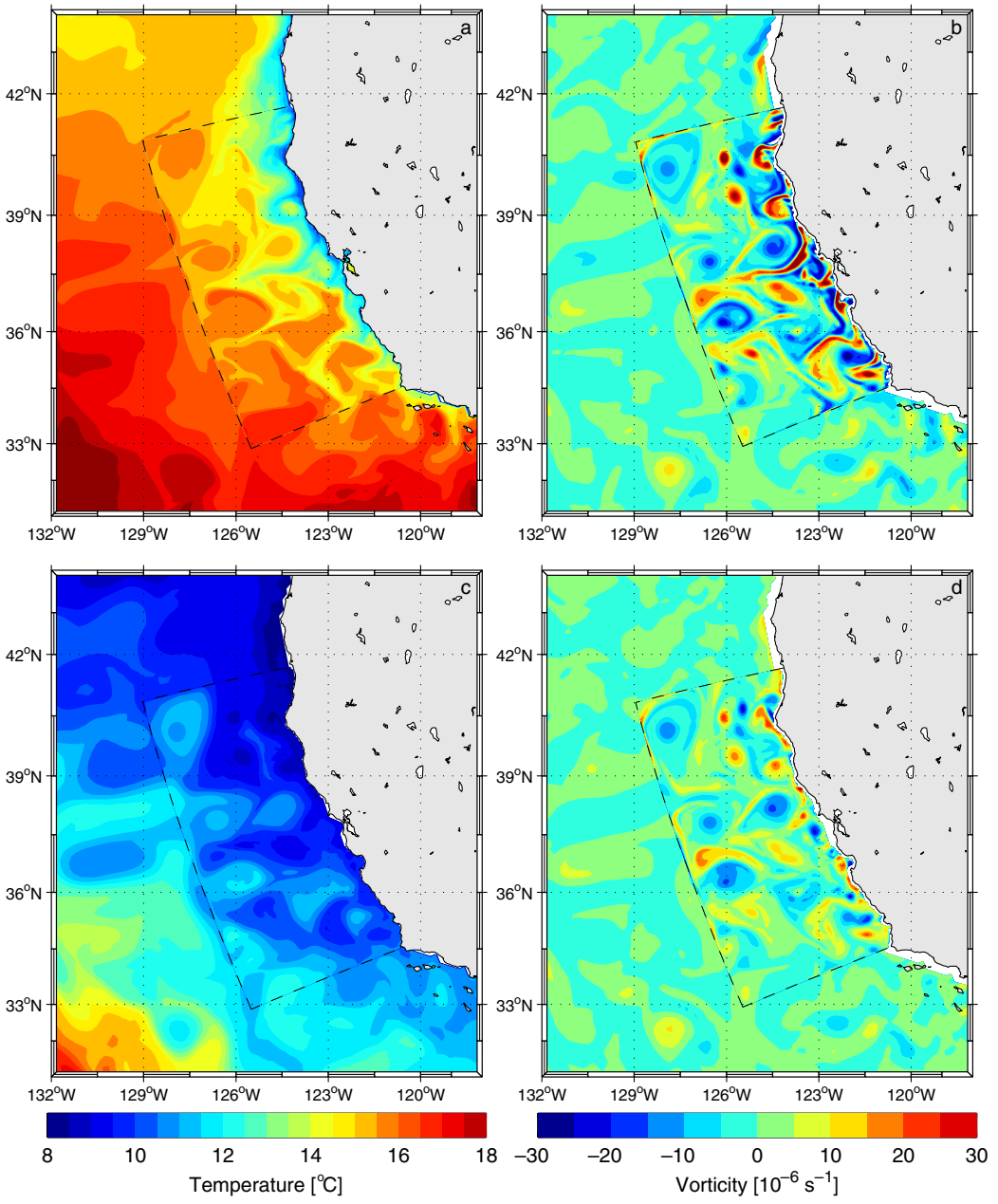

Fig. 6. Parent and child model solutions for 8 July of model year 5. (a) Sea-surface temperature (°C), (b) surface vorticity (s^{-1}), (c) temperature (°C) at 100 m depth, and (d) vorticity (s^{-1}) at 100 m depth.

of temperature, the child boundaries are almost unnoticeable. In the child solution, some filaments have extended to the Western boundary. Therefore, at these locations, because of the absence of feedback from the child to the parent model, discontinuities are apparent. Although reduced, this pattern is also evident at 100 m (Fig. 6c). The cross-boundary gradients of the along

boundary currents are represented by horizontal maps of the vertical component of vorticity (Fig. 6b and d). Close to the shore, instabilities in the upwelling jet induce a succession of cyclonic and anticyclonic eddies (Fig. 6b). For both surface and at 100 m depth, the typical value of vorticity for the eddies generated close to the shore is more than 2 to 3 times larger than the values observed on discontinuities at the child boundaries (Fig. 6b and d).

A vigorous eddy activity is present in the child model and is noticeable in Fig. 7, a series of sea-surface height images from December of year 9 to July of year 10. This image sequence presents the generation of mesoscale eddies via baroclinic and barotropic instabilities from the upwelling front in March, and their westward propagation (Marchesiello et al., 2003). One would expect more energetic eddies in the child domain than in the parent domain and at least be concerned about a barrier to their evacuation through the western boundary. A cyclonic eddy evacuates through the western boundary in Fig. 7. While there is no feedback from the child to the parent model, both solutions appear to be dynamically close enough to prevent the blocking of propagating structures at the child boundary.

Fig. 8 shows the time evolution of the model volume (Fig. 8a), the surface-averaged temperature (Fig. 8b), the volume-averaged temperature (Fig. 8c), the surface-averaged salinity (Fig. 8d), and the volume-averaged salinity (Fig. 8e). For each of these variables after a spin-up of 2 years, the parent and child models exhibit no significant temporal drift. In the case of fixed conditions at the child boundaries (dashed lines), there is an exact conservation of the volume flux at the

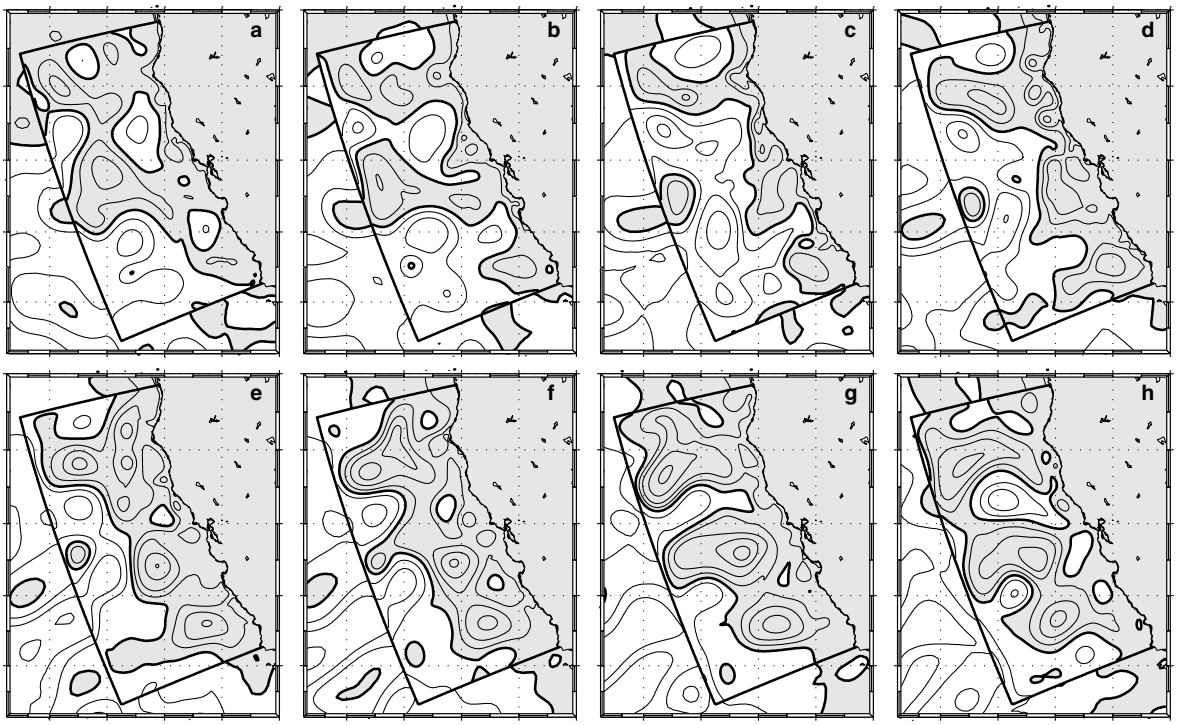

Fig. 7. From left to right and from top to bottom: sea-surface height (m) for (a) 15 December 9, (b) 15 January 10, (c) 15 February 10, (d) 15 March 10, (e) 15 April 10, (f) 15 May 10, (g) 15 June 10 and (h) 15 July 10.

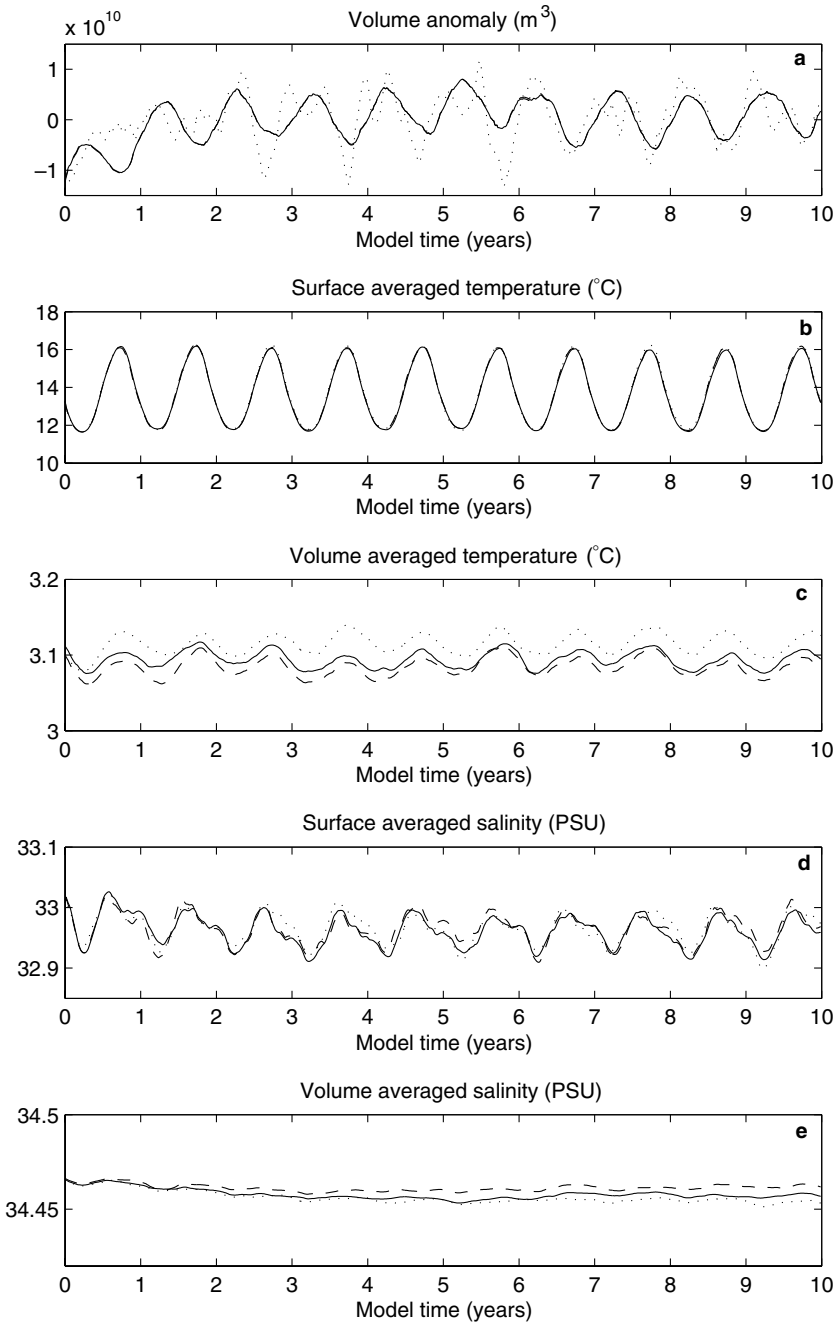

Fig. 8. Time evolution of different model variables. The plain line represents a subdomain of the parent model that covers the child grid; the dotted line represents the child model using the Flather boundary condition; and the dashed line represents the child model using clamped boundary conditions: (a) volume anomaly (m^3), the total volume is 1.4×10^{15} m^3, (b) surface averaged temperature (°C), (c) volume averaged temperature (°C), (d) surface averaged salinity (PSU), and (e) volume averaged salinity (PSU).

parent–child boundaries (Fig. 8a). The temperature is also conserved (Fig. 8b and c) as is the surface salinity (Fig. 8d). For the volume-averaged salinity, a slight difference arises (less than 0.01 PSU) between the parent and the child. This difference stabilizes after 2.5 years of simulation and does not significantly increase afterward. Volume flux is not exactly conserved in the case of Flather open-boundary conditions (dotted lines). Nevertheless, the inner-grid solution stays stable for multi-year solution with no significant increase (or decrease) of mass, heat, or salt. This validates the conservation properties of the interpolation methods employed in AGRIF and permits long-term embedded simulations without a significant drift of the mean properties of the child model in comparison to the parent.

3.3. Comparison of parent and child solutions

Does the higher resolution of the child domain bring an improvement in the solution in comparison to the low-resolution solution? The sea surface temperature is compared between the parent and the child model in Fig. 9. What is striking at first glance in these snapshots is the similarity of the solutions at large scale. Even the filaments appear to extend offshore from roughly the same locations (40.5°N–124.5°W, 39°N–124°W, 38°N–123°W, 37°N–122.5°W, 36.5°N–122°W). These locations corresponds to the major capes (Cape Mendocino, Point Arena, Point Reyes and Point Sur), supporting the idea that capes are efficient in anchoring the filament generation (Marchesiello et al., 2003). This might be a sign of good performance for the

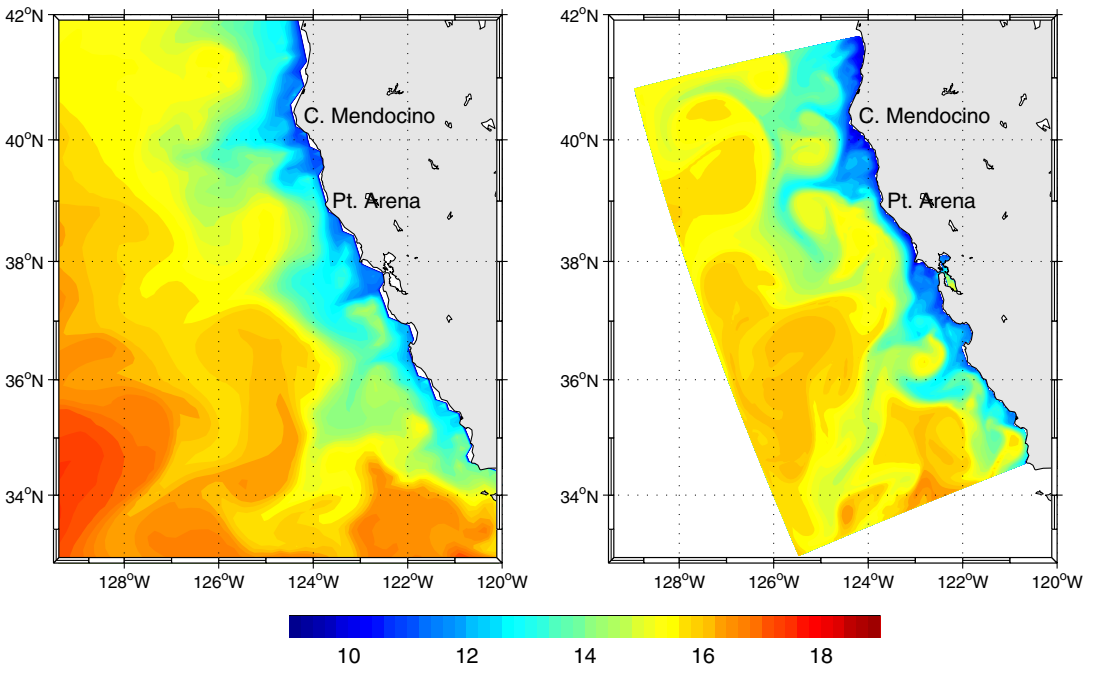

Fig. 9. Left: sea-surface temperature (°C) for 8 July of model year 10 for the parent model. Right: sea-surface temperature (°C) at the same moment for the child model. The color scale is the same for each image.

low-resolution model. Nevertheless, the child model develops stronger upwelling with colder water close to the shore. For this model the filaments are longer and narrower. Mushroom-like, warm structures (39°N–125°W and 36.5°N–122.5°W) appear to bring warm water toward the shore in agreement with the cross-shore eddy flux analyzed in Marchesiello et al. (2003). This results in a narrower upwelling front in the child model.

When comparing the annual mean sea-surface height for both grids (Fig. 10), we note the preservation of the large-scale mean circulation. While the meanders in the California Current appear at the same location in each model (associated with coastline indentations), they are definitely more pronounced in the child solution. Also, in the northern part of the child domain, the sea-surface elevation is steeper at the shore in the child than in the parent model. This can be related to the stronger upwelling observed at higher resolution.

While it does not affect dramatically the mean state of the solution, sufficient resolution is determinative for mesoscale variability. The annual standard deviation of sea-surface elevation is compared in Fig. 11 for the parent and the child model. For the child model, a maximum is present offshore with values more than 2 times stronger than for the parent model. The transition from the maximum to the lower parent values occurs progressively in a band of 50–100 km close to the child boundaries. The offshore maximum has also been observed in altimeter data and corresponds to the position of the California Current. Altimeter measurement and numerical modeling of the seasonal cycle of the California Current and eddy fields (Kelly et al., 1998; Strub and James, 2000; Haney et al., 2001), have shown that surface eddy kinetic energy is produced at the coast, in association to a surface intensified baroclinic jet during the upwelling season, and propagates offshore. This offshore propagation is accompanied by a diminution of eddy kinetic energy due

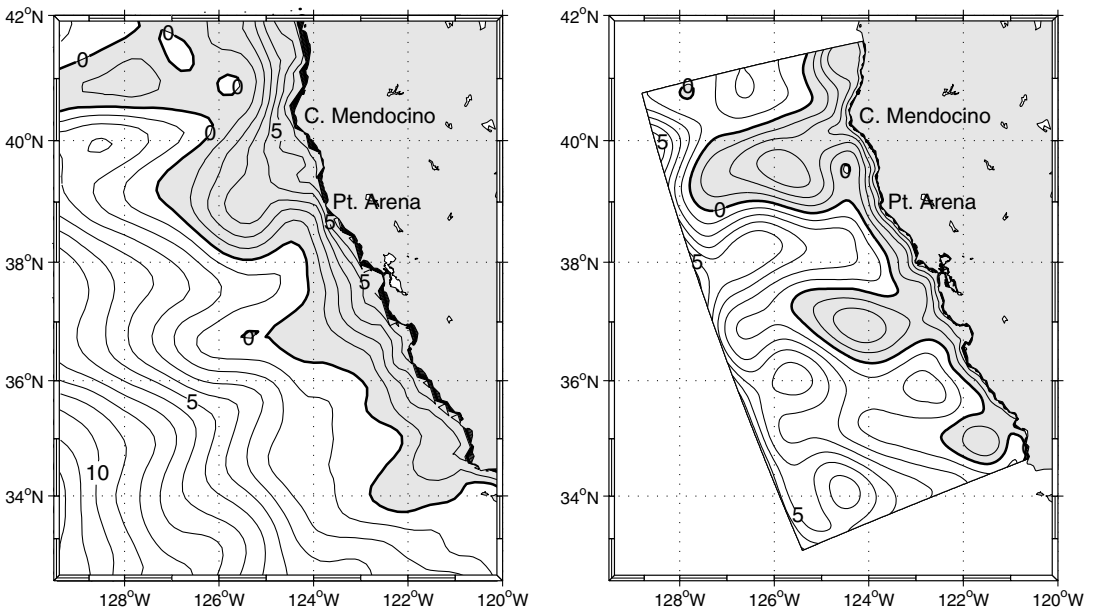

Fig. 10. Left: annual mean sea-surface height (m) for the parent model. Right: annual mean sea-surface height (m) for the child model.

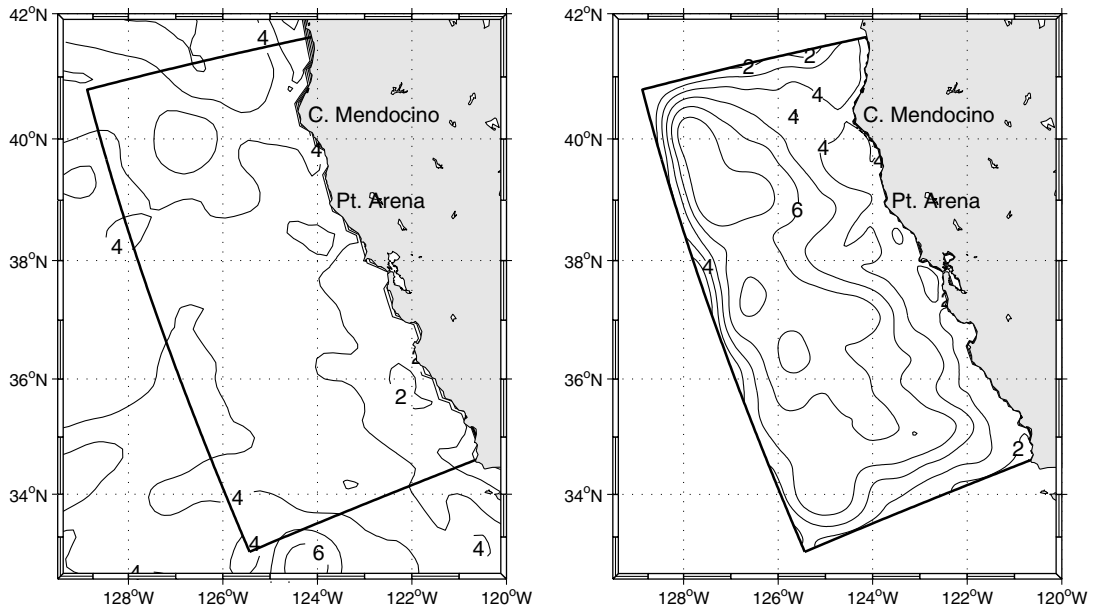

Fig. 11. Left: standard deviation of sea-surface elevation (m) for the parent model. Right: standard deviation of sea-surface elevation (m) for the child model.

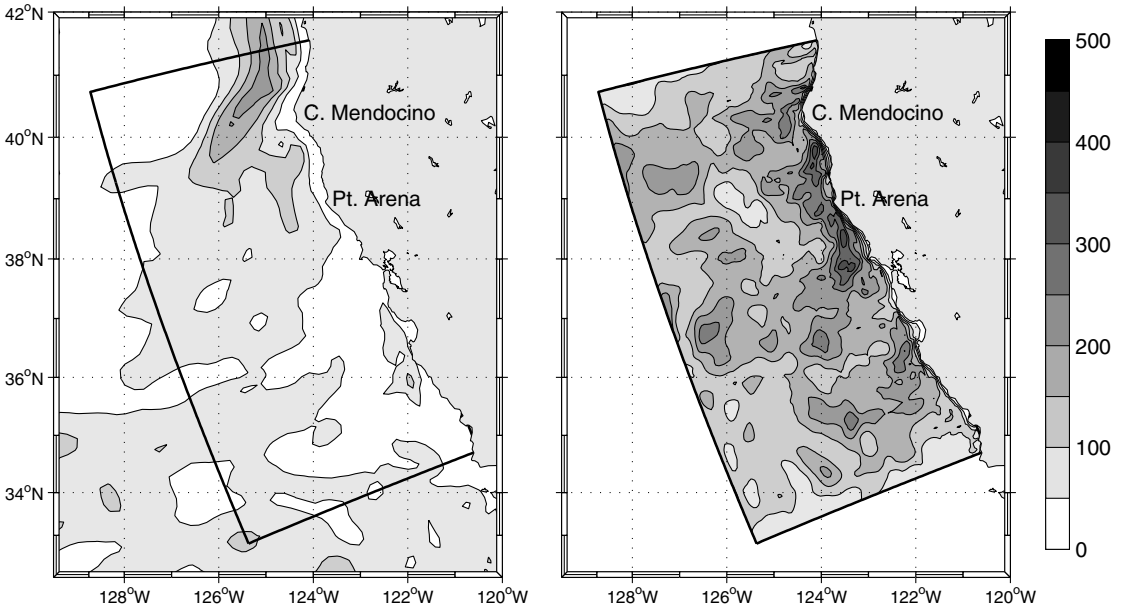

Fig. 12. Left: summer mean surface eddy kinetic energy ($cm^2\ s^{-2}$) for the parent model. Right: summer mean surface eddy kinetic energy ($cm^2\ s^{-2}$) for the child model.

to a barotropization of the eddies (Haney et al., 2001; Marchesiello et al., 2003). A comparison between the parent and the child models of the eddy kinetic energy in summer is provided on

Fig. 12. During the upwelling season, the maximum of eddy kinetic energy is located close to the shore for both models. Local maxima are situated near the major capes. But throughout the child domain, the level of summer eddy kinetic energy is more than 2 times higher than in the parent model. Close to the shore (in a coastal band about 100 km wide), it can be 4 to even more than 10 times higher. Hence, the child model is able to produce a level of eddy activity closer to what is observed in nature (see Marchesiello et al. (2003)).

4. 1-Way embedding evaluation

In the previous paragraph, we have seen that the child level produces a more energetic solution than the parent. But is a local zoom accurate enough in comparison to a large-scale solution at high resolution? And, as the complementary question, would open boundaries on a small domain alone, without embedding, suffice to produce equivalent results? Three other simulations are analyzed to address these questions. Firstly, a high-resolution model (5 km) of the whole Pacific Coast of the United States (USWC), fully described in Marchesiello et al. (2003), serves as a reference to test the capabilities of the embedding procedure. Secondly, two other models based on the child grid but using active/radiative open boundaries instead of embedding are set-up. A first one (called hereafter LEV) employs monthly mean climatological observations (Levitus and Boyer, 1994; Levitus et al., 1994) for the lateral boundary conditions. To test the influence of the large-scale mean state on the local solution, a second simulation (called hereafter CLIM) is constructed, employing a monthly climatology derived from USWC (i.e., a monthly time average) for its lateral boundary conditions. In CLIM, we are forcing the open boundaries using a dataset with the highest horizontal resolution available, filtering temporal variability (i.e., keeping solely the seasonal cycle). In the following text the embedded model of Section 3 is called EMB. All the other parameters in the four models are kept identical. For each simulation the solution is analyzed after a spin-up of 2 years, from year 3 to year 10.

In term of CPU cost, Table 2 shows the efficiency of the embedding procedure. Because of the shorter time step, the child grid is the most time consuming. The comparison between a reduced grid alone and EMB reveals that the time needed for data handling at the grid interfaces in AGRIF is negligible in front of the rest of the calculations. Hence, EMB is almost 8 times cheaper than USWC.

A snapshot of sea-surface temperature for the 1st of June of model year 6 for the four test experiments is portrayed in Fig. 13. This instant is typical of sea-surface temperature during the upwelling season. For this variable, the four experiments present strong similarities. They all show cold water (about 10 °C) at the shore, a narrow upwelling front (around 20 km) and

Table 2
CPU time in hours for 1 year of simulation for the different test cases of Monterey Bay area (using one R10000 195 MHz processor)

Whole US West Coast at 5 km	Whole US West Coast at 15 km	Reduced grid at 5 km	Embedded grids 15 km + 5 km
3000	60	320	380

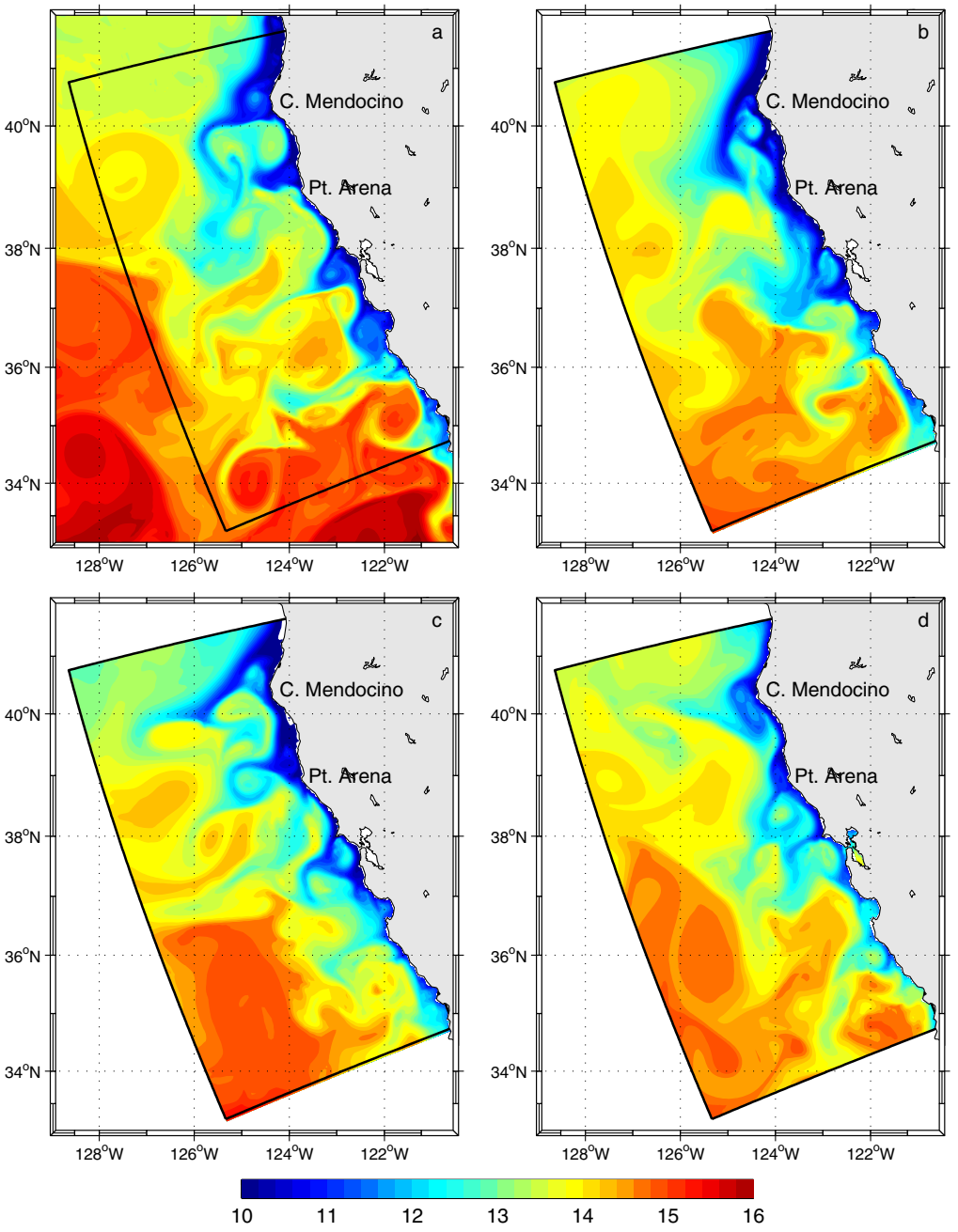

Fig. 13. Sea-surface temperature (°C) for the 8 June of model year 6 for the four test experiments ((a) USWC, (b) LEV, (c) CLIM, and (d) EMB).

warm water offshore (about 16–17 °C). The upwelling filaments have more or less the same length and width (perhaps slightly shorter for LEV), the warm intrusions toward the shore present the

same kind of mushroom like patterns, and the position of the upwelling front (about 50 km from the shore) is the same in each experiment, at least away from the lateral boundaries. The filaments appear to generate at approximately the same locations in all the experiments. The only significant differences are a smoother field near the boundaries and offshore for LEV and CLIM and the presence of warmer water coming from the south in USWC. From this type of picture, the upwelling and filament structure (at least the image in sea-surface temperature) seems to be mostly dependent on local processes (alongshore wind, an irregular shape in the coastline, instabilities, etc.), and large-scale dynamics does not seem to have a strong influence.

To check if the previous statement is also valid for the mean circulation in the California Current System, the annual average of sea-surface height is presented in Fig. 14. In each model, the sea-surface slopes account for a surface flow directed toward the equator showing large-scale meanders. In a band of 200 km close to the shore, the slopes are on average equivalent. But unlike sea-surface temperature, the gradient in the mean sea-surface height presents strong differences among the four experiments. The reference run (USWC) generates three large-scale, steady meanders like the standing eddies associated with coastline and topographic protrusions in Marchesiello et al. (2003). In LEV, the offshore boundary forces the sea-surface height gradients to stay rectilinear. It results in nearly a disappearance of the meanders, and only one is still present offshore of Monterey Bay. Although the boundaries in CLIM employ a monthly mean climatology of USWC data, the offshore mean response in CLIM is totally different to USWC. Inconsistencies between the boundary conditions and the inner solution result in unrealistic loops at the offshore boundary. This is a sign that the meanders observed in USWC could be a large-scale response generated by variations coming from the shore. EMB is definitely the closest to USWC. It exhibits three meanders at the same locations. The similarity between EMB and USWC degrades moving from the coast toward the offshore boundary. The strong intrusion of offshore water seen in USWC around 36°N and 126°W is present in neither of the other models.

One of the major difficulties in low-resolution models, and one of the expectations when increasing the resolution, is to get an accurate eddy variability. Measures of variability are presented in Fig. 15 for the standard deviation of sea-surface elevation, Fig. 16 for the annual surface eddy kinetic energy, and Fig. 17 for the summer surface eddy kinetic energy. For the standard deviation of the sea surface elevation (Fig. 15), USWC develops a maximum along the path of the California Current, about 300 km offshore. This maximum is still slightly lower than in the altimeter measurements (Marchesiello et al., 2003). It is almost nonexistent in LEV and in CLIM. These simulations failed to reproduce the variability of the offshore current. The standard deviation of sea-surface elevation for both of them is about two times lower than USWC and EMB. The similarity between LEV and CLIM reveals the low impact of the large-scale mean state on the variance of sea-surface elevation. The embedding allows EMB to produce a pattern close to USWC. Hence, to produce an accurate standard deviation of sea-surface elevation, one needs enough resolution at the shore (on Fig. 11 the parent model is not able to produce a correct level), but large-scale variations are also mandatory.

Since in the California Current System the eddies are mostly locally produced in the upwelling region, the influence of large-scale variations should be less noticeable for the level of eddy kinetic energy. On Figs. 16 and 17, one can note that the maximum of surface eddy kinetic energy is close to the shore in the vicinity the capes. LEV is more than 2 times lower than the 3 other experiments, but CLIM presents strong similarities with EMB away from the boundaries. This

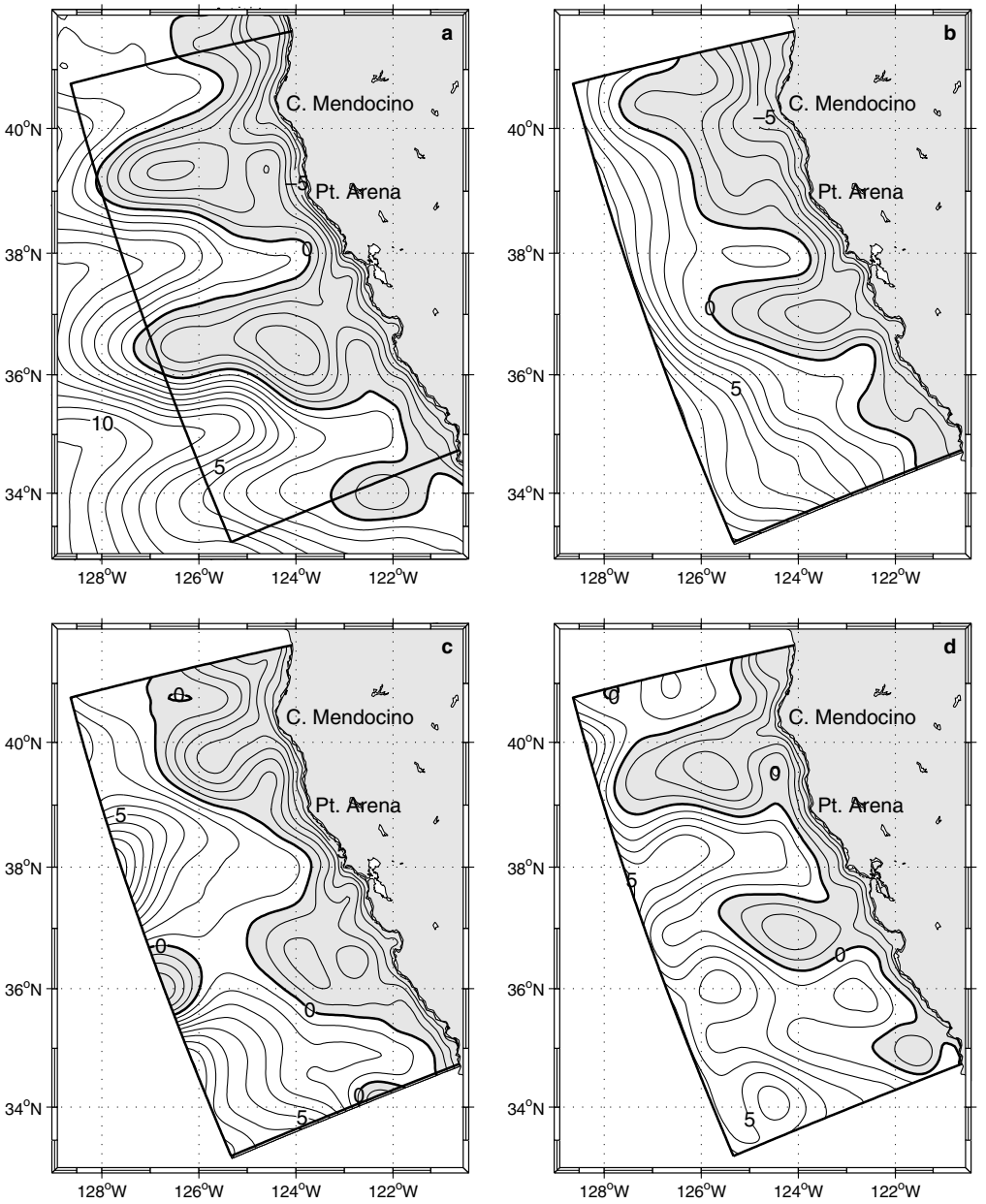

Fig. 14. Annual mean sea-surface height (cm) for the four test experiments ((a) USWC, (b) LEV, (c) CLIM, and (d) EMB).

reinforces the idea that the large-scale mean state (i.e., the mean structure of the upwelling front and/or the width and strength of the equatorward current) is important to obtain a correct level of eddy variability. A smooth climatology such as that employed for the boundaries in LEV cannot

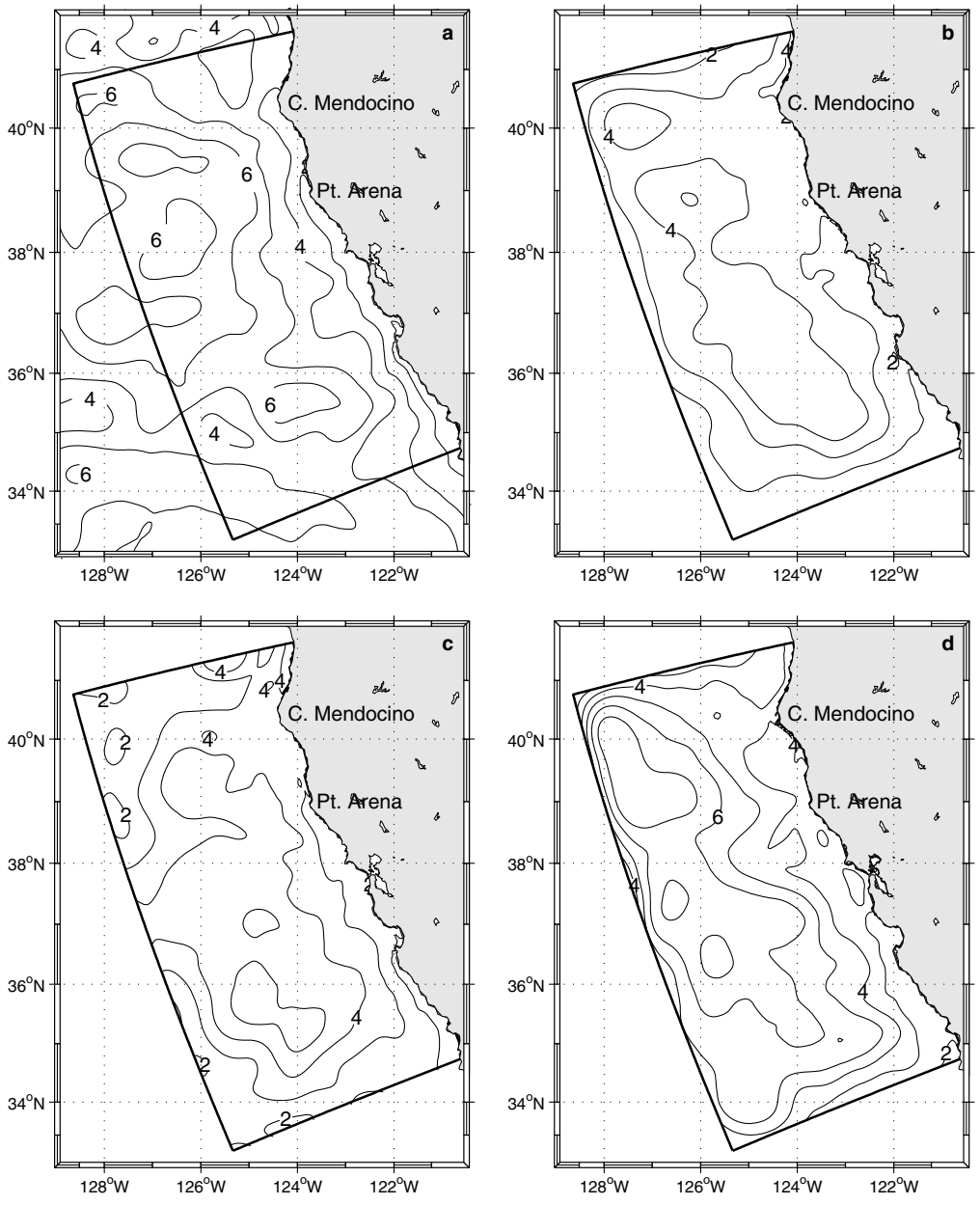

Fig. 15. Standard deviation of sea-surface elevation (cm) for the four test experiments ((a) USWC, (b) LEV, (c) CLIM, and (d) EMB).

provide an average state able to produce sufficient eddy variability in a domain as small as the inner domain here (i.e., 1000×500 km).

In this context, the eddy generation process in the California Current System appears to be a local process, but it could be remotely influenced by the mean current and hydrographic struc-

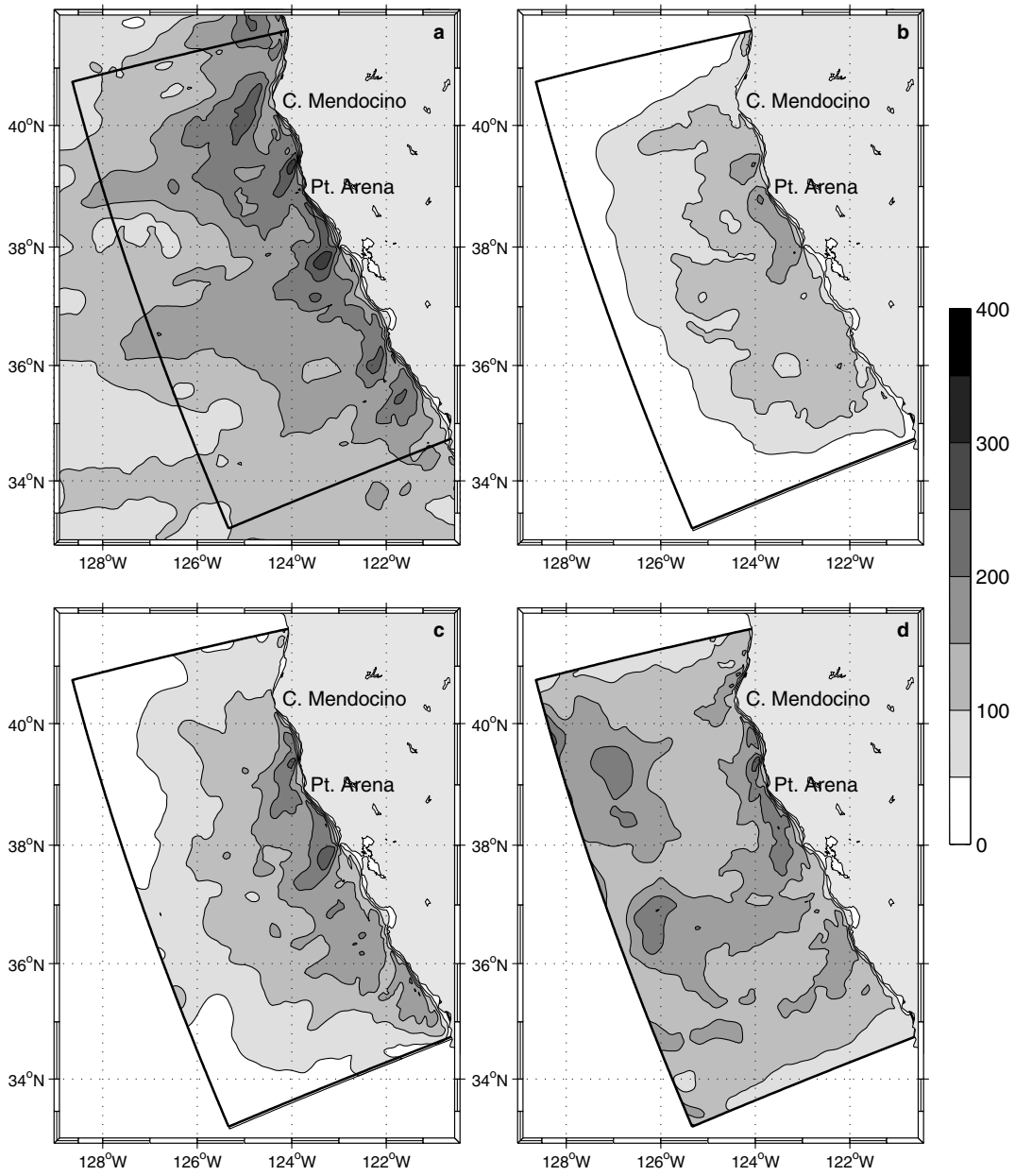

Fig. 16. Annual surface eddy kinetic energy ($cm^2\ s^{-2}$) for the four test experiments ((a) USWC, (b) LEV, (c) CLIM, and (d) EMB).

tures. Values of annual eddy kinetic energy for EMB resemble those of USWC (Fig. 16), but in summer, EMB present a level 25% lower in the coastal transition zone (Fig. 17). One can note in Fig. 17a that during this period, when the eddy activity is the strongest, high values can be observed in the northern part of the domain. This can be related to southward propagating eddies

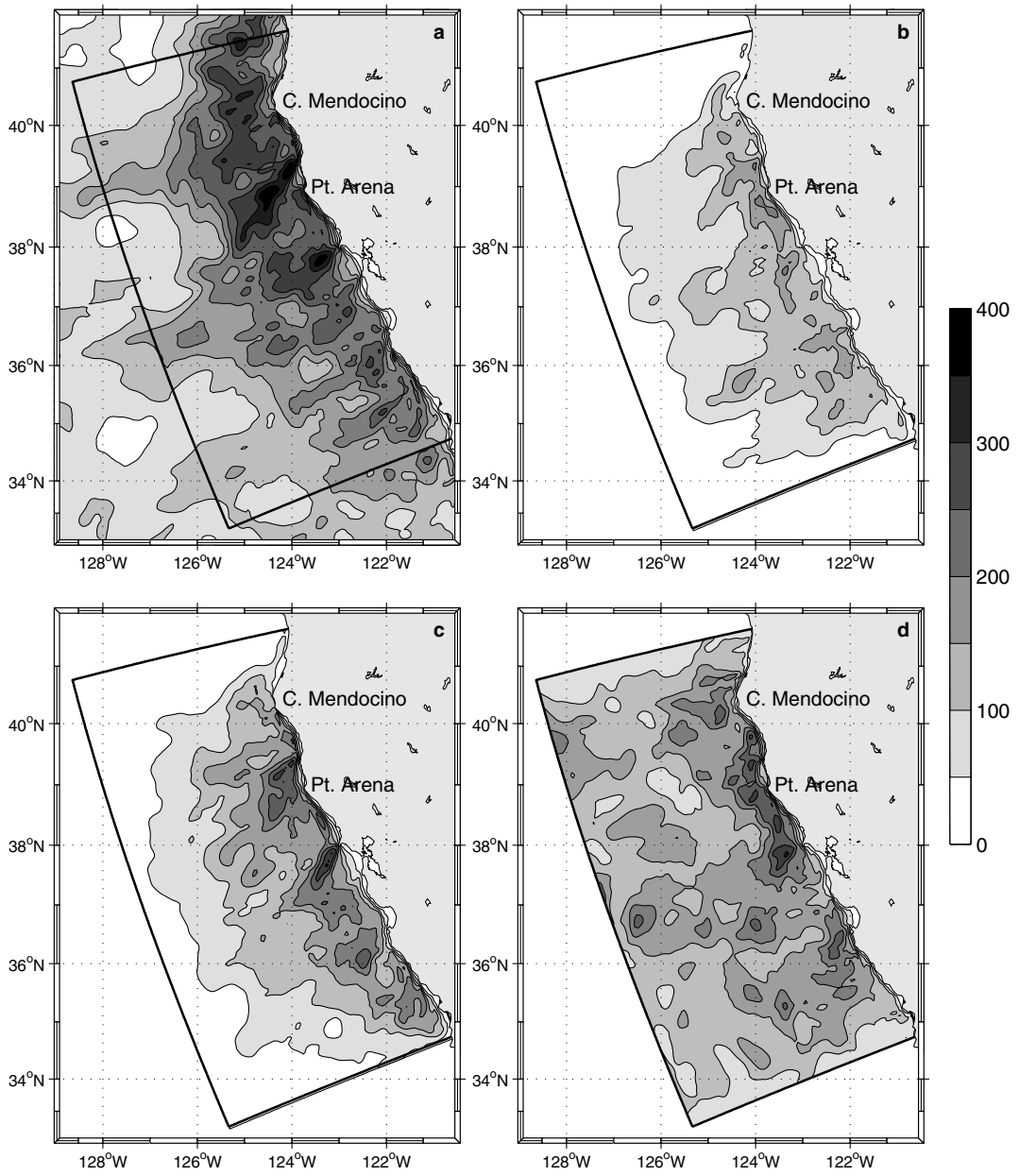

Fig. 17. Summer surface eddy kinetic energy ($cm^2\ s^{-2}$) for the four test experiments ((a) USWC, (b) LEV, (c) CLIM, and (d) EMB).

that are generated at Cape Blanco (43°N). As a matter of fact, Cape Blanco is recognized as a preferred site for coastal jet detachment and eddy generation (Barth and Smith, 1998). Not including this site within the child domain can explain the deficit of surface summer eddy kinetic energy in the embedded model.

5. Discussion

Using a 1-way embedding method, we obtained a high-resolution local solution at reasonable computational cost, while preserving the large-scale circulation. It required about 19 wall-clock hours on 16 processors of SGI Origin 2000 to compute 1 year of simulation, against 16 h for the child grid alone and 120 h for the whole Pacific coast at high resolution.

No important discontinuities where visible at the parent–child grid interface. The inner grid improved strongly the solution, especially the resolution of the mesoscale processes in comparison to the parent solution. The use of embedding also improved the solution in comparison to the utilization of open boundaries, even using finer data to force those boundaries. Hence, even if spatial resolution is coarser for the parent large-scale solution, bringing dynamically consistent external information at open boundaries (1-way embedding) considerably improves the inner-grid solution. While this it not immediately visible on images of sea-surface temperature, the improvement is dramatic when looking at the mean sea-surface elevation, the standard elevation of sea-surface height, and the eddy kinetic energy. Although it would have been interesting to extend the model evaluations to other variables, the choice has been made to use variables that are measurable by satellites, and therefore that can give a direct quantification of model performances. For each of these variables, the inner solution compares reasonably well to the whole pacific coast model solution at high resolution. Using 2-way embedding, the parent–child solutions should become even more dynamically consistent at the interface, increasing the overall accuracy (Clark and Hall, 1991). In the specific case of 2-way embedding, we presently are facing difficulties due to the complexity of the ROMS algorithmic structure, but we expect to resolve this issue in the very near future.

The comparison between solutions using different type of open boundaries brought also some insights about the dynamics of the California Current System. Hence, while the upwelling and filament structure seems to be mostly dependent on local processes, the meanders observed in the mean pathway of the California Current appears to be a large-scale response to mesoscale variations in the coastal transition zone. For the Central Upwelling off California, in the case of smooth climatological atmospheric forcing, variations in the large-scale circulation are needed for sufficient variance in sea-surface height. On the other hand, eddy variability appears mostly locally generated, but this process is strongly remotely influenced by the mean current and hydrographic structure. Also, in the case of the embedded model, the failure in resolving the eddies generated around Cape Blanco and propagating south in the domain could explain the deficit in surface eddy kinetic energy observed at the shore in summer.

A graphic users interface, part of the ROMSTOOLS package developed in the Institut de Recherche pour le Développement, facilitates the generation of embedded models (Penven, 2003). Therefore the embedding procedure is flexible in its use, allowing a rapid investigation of regional small-scale processes or specific domains. The multiplication of levels of embedding can also be used to address very fine-scale problems or to study the response of coastal regions to large-scale climate variations such as El Niño—Southern Oscillation and Pacific Decadal Oscillation.

Acknowledgment

This research was partially supported by the Office of Naval Research grant N00014-00-1-0249.

References

Barth, J.A., Smith, R.L, 1998. Separation of a coastal upwelling jet at Cape Blanco, Oregon, USA. South African Journal of Marine Science 19, 5–14.

Blayo, E., Debreu, L., 1999. Adaptive mesh refinement for finite-difference ocean models: first experiments. Journal of Physical Oceanography 29, 1239–1250.

Blayo, E., Debreu, L., 2005. Revisiting open boundary conditions from the point of view of characteristic variables. Ocean Modelling 9, 231–252.

Clark, T.L., Hall, W.D., 1991. Multi-domain simulations of the time dependent Navier–Stokes equations: Benchmark error analysis of some nesting procedures. Journal of Computational Physics 92, 456–481.

Cushman-Roisin, B., Naimie, C.E, 2002. A 3D finite-element model of the Adriatic tides. Journal of Marine Systems 37, 279–297.

Da Silva, A.M., Young, C.C., Levitus, S., 1994. Atlas of Surface Marine Data 1994, Vol. 1, Algorithms and Procedures, NOAA Atlas NESDIS 6, U.S. Department of Commerce, NOAA, NESDIS, USA, 74 pp.

Debreu, L., 2000. Raffinement adaptatif de maillage et méthodes de zoom—application aux modèles d'océan, 2000, Ph.D. thesis, Université Joseph Fourier, Grenoble.

Debreu, L., Blayo, E., 2003. AGRIF: Adaptive Grid Refinement In Fortran. Submitted to ACM Transactions on Mathematical Software—TOMS.

Debreu, L., Vouland, C., 2003. AGRIF: Adaptive Grid Refinement in Fortran. [Available online http://www-lmc.imag.fr/IDOPT/AGRIF/index.html].

Dudhia, J., Bresch, J.F., 2002. A Global Version of the PSU NCAR Mesoscale Model. Monthly Weather Review 130, 2989–3007.

Flather, R.A., 1976. A tidal model of the northwest European continental shelf. Mémoires de la Société Royale des Sciences de Liège 10, 141–164.

Fox, A.D., Maskell, S.J., 1995. Two-way interactive nesting of primitive equation ocean models with topography. Journal of Physical Oceanography 25, 2977–2996.

Ginis, I., Richardson, R.M., Rothstein, L.M., 1998. Design of a multiply nested primitive equation ocean model. Monthly Weather Review 126, 1054–1079.

Guo, X., Hukuda, H., Miyazawa, Y., Yamagata, T., 2003. A triply nested ocean model for simulating the Kuroshio—roles of horizontal resolution on JEBAR. Journal of Physical Oceanography 33, 146–169.

Haney, R.L., 1991. On the pressure force over steep topography in sigma coordinate ocean models. Journal of Physical Oceanography 21, 610–619.

Haney, R.L., Hale, R.A., Dietrich, D.E., 2001. Offshore propagation of eddy kinetic energy in the California Current. Journal of Geophysical Research 106, 11,709–11,717.

Hannah, C.G., Shore, J.A., Loder, J.W., Naimie, C.E., 2001. Seasonal circulation on the western and central Scotian Shelf. Journal of Physical Oceanography 31, 591–615.

Heggelund, Y., Berntsen, J., 2002. A method for analysing nesting techniques for the linearized shallow water equations. International Journal for Numerical Methods in Fluids 38, 163–185.

Herrnstein, A., Wickett, M., Rodrigue, G., 2005. Structured adaptive mesh refinement using leapfrog time integration on a staggered grid for ocean models. Ocean Modelling 9, 283–304.

Hervouet, J.-M., 2000. TELEMAC modeling system: an overview. Hydrological Processes 14, 2209–2210.

Iskandarani, M., Haidvogel, D.B., Levin, J.C., 2003. A three-dimensional spectral element model for the solution of the hydrostatic primitive equations. Journal of Computational Physics 186, 397–425.

Kelly, K.A., Beardsley, R.C., Limeburner, R., Brink, K.H., Paduan, J.D., Chereskin, T.K., 1998. Variability of the near-surface eddy kinetic energy in the California Current based on altimetric, drifter, and moored current data. Journal of Geophysical Research 103, 13,067–13,083.

Kurihara, Y., Tripoli, G.J., Bender, M.A., 1979. Design of a movable nested-mesh primitive equation model. Monthly Weather Review 107, 239–249.

Large, W.G., McWilliams, J.C., Doney, S.C., 1994. Oceanic vertical mixing: a review and a model with a nonlocal boundary layer parameterization. Reviews in Geophysics 32, 363–403.

Levitus, S., Boyer, T.P., 1994. World Ocean Atlas 1994, vol. 4: Temperature. NOAA Atlas NESDIS 4, US Government Printing Office, Washington, DC, 117 pp.

Levitus, S., Burget, R., Boyer, T.P., 1994. World Ocean Atlas 1994, vol. 3: Salinity. NOAA Atlas NESDIS 3, US Government Printing Office, Washington, DC, 99 pp.

Lynch, D.R., Naimie, C.E., Werner, F.E., 1996. Comprehensive coastal circulation model with application to the Gulf of Maine. Continental Shelf Research 16, 851–875.

Marchesiello, P., McWilliams, J.C., Shchepetkin, A., 2001. Open boundary condition for long-term integration of regional oceanic models. Ocean Modelling 3, 1–21.

Marchesiello, P., McWilliams, J.C., Shchepetkin, A., 2003. Equilibrium structure and dynamics of the California Current System. Journal of Physical Oceanography 33, 753–783.

Naimie, C.E., 1996. Georges Bank residual circulation during weak and strong stratification. Journal of Geophysical Research 101, 6469–6486.

Oey, L.-Y., Chen, P., 1992. A nested-grid ocean model: with application to the simulation of meanders and eddies in the Norwegian Coastal Current. Journal of Geophysical Research 97, 20,063–20,086.

Penven, P., 2003. ROMSTOOLS user's guide http://www.brest.ird.fr/roms_tools, Technical report, Institut de Recherche pour le Développement, 213 rue Lafayette, Paris, France.

Perkins, A.L., Smedstad, L.F., Blake, D.W., Heburn, G.W., Wallcraft, A.J., 1997. A new nested boundary condition for a primitive-equation ocean model. Journal of Geophysical Research 102, 3483–3500.

Perkins, A.L., Smedstad, L.F., 1998. Scale-related aspects of nested finite difference ocean models. Theoretical and Computational Fluid Dynamics 10, 311–322.

Sanderson, B.G., 1998. Order and resolution for computational ocean dynamics. Journal of Physical Oceanography 28, 1271–1286.

Shchepetkin, A.F., McWilliams, J.C., 1998. Quasi-monotone advection schemes based on explicit locally adaptive dissipation. Monthly Weather Review 126, 1541–1580.

Shchepetkin, A.F., McWilliams, J.C., 2003. A method for computing horizontal pressure-gradient force in an ocean model with a non-aligned vertical coordinate. Journal of Geophysical Research 108 (C3), 3090.

Shchepetkin, A.F., McWilliams, J.C., 2005. Regional Ocean Model System: a split-explicit ocean model with a free-surface and topography-following vertical coordinate. Ocean Modelling 9, 347–404.

Slørdal, L.H., Martinsen, E.A., Blumberg, A.F., 1994. Modeling the response of an idealized coastal ocean to a traveling storm and to flow over bottom topography. Journal of Physical Oceanography 24, 1689–1705.

Smith, W.H.F., Sandwell, D.T., 1997. Global seafloor topography from satellite altimetry and ship depth soundings. Science 277, 1957–1962.

Spall, M.A., Holland, W.R., 1991. A nested primitive equation model for oceanic applications. Journal of Physical Oceanography 21, 205–220.

Stein, J., Richard, E., Lafore, J.P., Pinty, J.P., Asencio, N., Cosma, S., 2000. High-resolution non-hydrostatic simulations of flash-flood episodes with grid-nesting and ice-phase parametrization. Meteorology and Atmospheric Physics 72, 101–110.

Strub, P.T., James, C., 2000. Altimeter-derived variability of surface velocities in the California Current System. 2. Seasonal circulation and eddy statistics. Deep Sea Research Part II 47, 831–870.

Walko, R.L., Tremback, C.J., 2000. Introduction to RAMS. [Available online http://www.aster.com/rams.shtml].